Mon. Not. R. Astron. Soc. **000**, 1–20 (2012) Printed 4 March 2013 (MN LATEX style file v2.2)

# Galactic star formation and accretion histories from matching galaxies to dark matter haloes

Benjamin P. Moster ⋆, Thorsten Naab, Simon D. M. White
*Max-Planck Institut für Astrophysik, Karl-Schwarzschild Straße 1, 85748 Garching, Germany*

arXiv:1205.5807v1 [astro-ph.CO] 25 May 2012

4 March 2013

**ABSTRACT**

We present a new statistical method to determine the relationship between the stellar masses of galaxies and the masses of their host dark matter haloes over the entire cosmic history from $z \sim 4$ to the present. This multi-epoch abundance matching (MEAM) model self-consistently takes into account that satellite galaxies first become satellites at times earlier than they are observed. We employ a redshift-dependent parameterization of the stellar-to-halo mass relation to populate haloes and subhaloes in the Millennium simulations with galaxies, requiring that the observed stellar mass functions at several redshifts be reproduced simultaneously. We show that physically meaningful growth of massive galaxies is consistent with these data only if observational mass errors are taken into account. Using merger trees extracted from the dark matter simulations in combination with MEAM, we predict the average assembly histories of galaxies, separating into star formation within the galaxies (in-situ) and accretion of stars (ex-situ). Our main results are: The peak star formation efficiency decreases with redshift from 23 per cent at $z = 0$ to 9 per cent at $z = 4$ while the corresponding halo mass increases from $10^{11.8} M_\odot$ to $10^{12.5} M_\odot$. The star formation rate of central galaxies peaks at a redshift which depends on halo mass; for massive haloes this peak is at early cosmic times while for low-mass galaxies the peak has not been reached yet. In haloes similar to that of the Milky-Way about half of the central stellar mass is assembled after $z = 0.7$. In low-mass haloes, the accretion of satellites contributes little to the assembly of their central galaxies, while in massive haloes more than half of the central stellar mass is formed ex-situ with significant accretion of satellites at $z < 2$. We find that our method implies a cosmic star formation history and an evolution of specific star formation rates which are consistent with those inferred directly. We present convenient fitting functions for stellar masses, star formation rates, and accretion rates as functions of halo mass and redshift.

**Key words:** cosmology: dark matter, theory – galaxies: evolution, high-redshift, statistics, stellar content

## 1 INTRODUCTION

Modern large-scale dark matter simulations are able to make accurate and definite predictions for the properties of dark matter haloes at all cosmic epochs in cold dark matter (CDM) cosmologies (Springel et al. 2005; Boylan-Kolchin et al. 2008; Klypin et al. 2011; Angulo et al. 2012). In this framework, galaxy formation is driven by the growth of the underlying large-scale structure and the formation of dark matter haloes: galaxies form by the cooling and condensation of gas at the centres of the potential wells of such dark matter haloes (White & Rees 1978; Fall & Efstathiou 1980). This results in a tight correlation between the physical properties of galaxies, such as their stellar mass and star formation rate (SFR), and the mass of the haloes by which they are hosted.

Galaxy formation studies have adopted several approaches to link galaxy properties to those of the dark matter haloes. The most direct is to model the physical mechanisms that drive the formation of galaxies from first principles. Here, an $N$-body treatment of the dark matter evolution is combined with a treatment of the baryonic component based either on a hydrodynamical (Katz et al. 1996; Springel & Hernquist 2003;

⋆ moster@mpa-garching.mpg.de

Kereš et al. 2005; Crain et al. 2009; Schaye et al. 2010; Oppenheimer et al. 2010) or on a semi-analytic method (Kauffmann et al. 1999; Springel et al. 2001; Hatton et al. 2003; Springel et al. 2005; Kang et al. 2005; Croton et al. 2006; Bower et al. 2006; Guo et al. 2011). Despite substantial progress, simplified and uncertain recipes must still be employed to model the formation of stars and black holes and the associated feedback processes, and the detailed properties and evolution of observed galaxy populations are still only partially reproduced.

An alternative approach to link galaxies to haloes has emerged with the accumulation of data from large galaxy surveys (Cole et al. 2001; Bell et al. 2003; Drory et al. 2005; Fontana et al. 2006; Panter et al. 2007; Pérez-González et al. 2008; Li & White 2009; Santini et al. 2012). Instead of attempting to model the baryonic physics that drive galaxy formation, dark matter haloes are populated with galaxies using a simple empirical method with adjustable parameters. In the popular halo occupation distribution (HOD) formalism, the distribution of galaxies (having certain intrinsic properties such as luminosity, color, or type) within main haloes of a given mass is constrained using galaxy abundance and clustering statistics (e.g. Peacock & Smith 2000; White 2001; Berlind & Weinberg 2002; Zehavi et al. 2004; Tinker et al. 2005; Brown et al. 2008; Zehavi et al. 2011; Wake et al. 2011; Leauthaud et al. 2012). A variant of the classical HOD approach is the conditional luminosity function (CLF) formalism (Yang et al. 2003; van den Bosch et al. 2003; Yang et al. 2011). Since reliable galaxy clustering measurements are unavailable at high redshift, the HOD and CLF approaches have typically been used at low redshift.

In order to circumvent this problem, galaxies can be linked to the underlying substructure directly by assuming a monotonic relation between stellar mass and halo mass, and matching the cumulative abundance of galaxies to those of haloes and subhaloes (Vale & Ostriker 2004; Conroy et al. 2006; Shankar et al. 2006; Vale & Ostriker 2006; Moster et al. 2010; Guo et al. 2010; Behroozi et al. 2010). The only observational input to this 'abundance matching' method is thus the observed stellar mass function (SMF) or luminosity function. This approach then predicts clustering statistics remarkably well. In this framework, the stellar-to-halo-mass (SHM) relation can be obtained in two ways: The first (e.g. Conroy et al. 2006) is to create a mock galaxy catalogue from the observed SMF for the simulated volume, to order both galaxies and haloes by mass, and then to match them one by one. A fitting function can then be used to get the SHM relation. The second way (e.g. Moster et al. 2010) is first to assume a functional form for the SHM relation, and then to populate the haloes with galaxies and compute the model SMF. The parameters of the SHM function are then adjusted so that the observed SMF is reproduced. The latter approach has the advantage that scatter in stellar mass at a given halo mass can easily be added.

The underlying assumptions in this model are that satellite galaxies are living in subhaloes and were central galaxies before their own haloes were accreted and became subhaloes. The properties of the galaxy population today are thus a consequence of the formation of central galaxies in main haloes at different redshifts and the subsequent accretion and evolution of satellites. Since the subhalo is affected much more by tidal stripping than the galaxy at its centre, the stellar mass of satellites is more closely related to subhalo mass at the time of accretion rather than to current subhalo mass. Most abundance matching studies simply assign the infall mass to subhaloes. As pointed out by Yang et al. (2011), this is equivalent to assuming that the SHM relation does not evolve with redshift, i.e. that the relation between the stellar mass of central galaxies and their halo mass today is the same as the relation between the stellar mass of satellite galaxies and their halo mass at the time of accretion. However, applying the technique at different redshifts results in an evolving SHM relation (e.g. Conroy et al. 2006; Moster et al. 2010). This indicates that the classical abundance matching approach is not self-consistent.

This problem can be solved if we assign the stellar mass of the satellites depending on the infall mass of their subhalo *and* the infall redshift. The stellar mass of the central galaxies still depends on the main halo mass at the redshift of observation in the same way. This is equivalent to assuming that the stellar mass of a satellite does not change, once it has entered the main halo. In order to implement this scheme, we first use the classical abundance matching approach to see how the parameters of the SHM relation depend on redshift and find a redshift-dependent parameterization of the SHM relation $m_*(M_\mathrm{h}, z)$. We then employ this parameterization to put a galaxy at the centre of every halo and subhalo in the simulation at all redshifts between $z = 0$ and $z = 4$, adjusting the parameters of the relation to reproduce simultaneously all the observed SMFs in this redshift range. In this way we use a self-consistent relation between stellar mass, halo mass and redshift for both centrals and satellites.

Statistical models, such as the abundance matching approach, are typically employed to derive constraints on the relation between galaxy properties and halo mass at a given epoch. With the advent of wide high-redshift surveys, it has become possible to use this connection, together with information on the evolution of dark matter haloes, to study the evolution of galaxy properties throughout their history (e.g. White et al. 2007; Conroy et al. 2007). In particular, Conroy & Wechsler (2009) show how this method can be extended to put constraints on the SFR of galaxies. For this they use an analytic prescription for galaxy and halo abundances and the evolution of haloes, focusing on $z \lesssim 1$. We follow a similar approach, but use $N$-body simulations to get halo abundances and assembly histories. Then we identify the progenitors of a given halo at an earlier epoch and derive the amount of stellar mass that has been accreted onto the central galaxy and the total stellar mass by which it grew. Finally, employing a recipe to account for stellar mass loss, we compute the stellar mass that has been formed through star formation and convert this into a SFR. We are thus able to derive the star formation history (SFH) of the galaxy at the centre of the halo.

This paper is organized as follows. In Section 2, we describe the $N$-body simulations including the halo finding algorithm and the treatment of 'orphan' galaxies. We also summarize the observational SMFs that have been used. In Section 3 we describe the details of the model that matches galaxies to haloes. In Section 4 we use this relation and the halo accretion histories to derive SFR histories as a function

of halo mass and we show that our model can reproduce the observed evolution of the cosmic SFR density and of the specific SFRs of galaxies. We discuss some of the implications of our model in Section 5 and summarize in Section 6.

Throughout this paper, we assume a '*WMAP7*' ΛCDM cosmology with $(\Omega_{\rm m}, \Omega_\Lambda, \Omega_{\rm b}, h, n, \sigma_8) = (0.272, 0.728, 0.046, 0.704, 0.967, 0.810)$. We employ a Chabrier (2003) initial mass function (IMF) and we convert all stellar masses to this IMF. All virial masses are computed with respect to 200 times the critical density. In order to simplify the notation, we will use the capital $M$ to denote dark matter halo masses and the lower case $m$ to denote galaxy stellar masses.

## 2 SIMULATIONS AND OBSERVATIONS

In this paper we aim to link observable properties of galaxies to the underlying dark matter distribution using a statistical sample of both galaxies and dark matter haloes. The properties of the halo population originate from two $N$-body simulations: the Millennium Simulation (MS Springel et al. 2005) for massive haloes and the Millennium-II Simulation (MS-II Boylan-Kolchin et al. 2009) for lower mass haloes.

For the galaxy population at low redshift we use the precise stellar mass functions of Li & White (2009) based on the spectroscopic data set of the Sloan Digital Sky Survey (SDSS York et al. 2000). At high redshift we use two sets of observed SMFs: for massive galaxies we use the SMFs by Pérez-González et al. (2008, PG08) taken from a wide survey, and for low-mass galaxies we use the SMFs by Santini et al. (2012, S12) taken from a deep survey.

### 2.1 Numerical Simulations

Both Millennium simulations adopt the concordance ΛCDM cosmology with parameters chosen to agree with the first-year *Wilkinson Microwave Anisotropy Probe* (*WMAP*) data (Spergel et al. 2003). As these parameters are not consistent with the latest *WMAP* data analysis, we use the scaling recipe by Angulo & White (2010) to convert the properties of the simulations to represent the growth of structure in a *WMAP7* cosmology. Specifically, we chose $\Omega_{\rm m} = 0.272$, $\Omega_\Lambda = 0.728$, $\Omega_{\rm b} = 0.0455$, $H_0 = 70.4$ km s$^{-1}$ Mpc$^{-1}$, $n = 0.967$ and $\sigma_8 = 0.81$ (Komatsu et al. 2011).

Both simulations were carried out in a periodic box advancing $2160^3$ dark matter particles from redshift $z \sim 127$ to 0. The side length of the box is 761 Mpc for the *MS*, and 152 Mpc for the *MS-II*. The corresponding particle masses are $1.58 \times 10^9 M_\odot$ and $1.27 \times 10^7 M_\odot$, respectively. The large volume of the *MS* enables us to sample reliably even the central galaxies of rare and massive clusters, while the *MS-II* has sufficient resolution to sample the faintest dwarf galaxies.

Dark matter haloes are identified at each output using a friends-of-friends (FoF) halo finder that links together particles with separation less than 0.2 of the mean interparticle distance. Substructures inside the FoF groups are then identified using SUBFIND (Springel et al. 2001). The most massive self-bound subgroup is defined as the 'main halo', and all other subgroups within the FoF groups are referred to as 'subhaloes'. The virial radius and mass of the main haloes are determined with a spherical overdensity criterion: the density inside a sphere centered on the most bound particle is required to be equal to 200 times the critical value. Merger trees were then built to link each subhalo found at a given snapshot (including the main haloes) to a unique descendant in the following snapshot. With these merger trees we can track the evolution of each halo throughout the simulation.

In this work, we assume that both main haloes and subhaloes host galaxies at their centres. We will refer to the galaxy at the center of a distinct halo as a 'central galaxy', and the galaxies within subhaloes as 'satellites'. There is thus one central galaxy within each FoF group but there may be any number of sattelites (including zero). Ab initio models of galaxy formation predict that the stellar mass of a galaxy is tightly correlated with the depth of the potential well of the halo in which it formed. For central galaxies, the relevant mass is the virial mass of the main halo at the time of observation, but for satellites the situation is more complex: Subhaloes lose mass while orbiting in a larger system as their outer regions are tidally stripped. Stars are centrally concentrated and more tightly bound than the dark matter, however, so the stellar mass of a satellite galaxy changes only slightly after it enters a larger halo. Therefore the subhalo mass at the time of observation is not a good tracer for the stellar mass of a satellite. A better tracer is the subhalo mass at the time that it was accreted by the main halo, which typically corresponds to the maximum mass over its history.

Due to the finite mass resolution of the simulations, subhaloes can no longer be identified once their mass has been tidally stripped below the resolution limit. Since mass loss can be substantial this is important even for fairly massive subhaloes. A special treatment of these so-called 'orphans' is necessary. We determine the orbital parameters the last time a subhalo is identified in the simulation and use them in the dynamical friction formula of Binney & Tremaine (1987):

$$t_{\rm df} = \alpha_{\rm df} \frac{V_{\rm vir} r_{\rm sat}^2}{G M_{\rm sat} \ln \Lambda} \,, \qquad (1)$$

where $r_{\rm sat}$ is the distance between the centers of the main halo and of the subhalo at the time the merger clock was set, $M_{\rm sat}$ is the mass of the subhalo at this time, and $\ln \Lambda = \ln(1 + M_{\rm vir}/M_{\rm sat})$ is the Coulomb logarithm. Following De Lucia & Blaizot (2007) we set $\alpha_{\rm df} = 2.34$, which was also found to be appropriate in the $N$-body studies by Boylan-Kolchin et al. (2008). We retain the disrupted subhalo for the purposes of abundance matching until a time $t_{\rm df}$ has elapsed, and assume that only then does it truly merge with the main halo.

### 2.2 Observed stellar mass functions

Having derived the abundance of the halo/subhalo population as a function of mass and redshift, we now have to select samples of observed galaxy abundances, to link the two populations. At low redshift ($z = 0.1$), the SDSS galaxy catalogues allow a determination of the local SMF down to a stellar mass of $10^7 M_\odot$. Above about $10^8 M_\odot$ it is robust against incompleteness. The large volume of the sample leads to very low uncertainties due to cosmic variance (Trenti & Stiavelli 2008; Moster et al. 2011).

We employ the recent measurements by Li & White

(2009), based on a complete and uniform sample from the SDSS/DR7 (Abazajian et al. 2009), and we use the conversion to stellar mass based on the SDSS $r$-band model luminosities, as derived by Guo et al. (2010). This SMF ranges from stellar masses of $10^{8.3} M_\odot$ to $10^{11.7} M_\odot$. In order to extend the SMF to even lower stellar masses, we include the measurements by Baldry et al. (2008) between $10^{7.4} M_\odot$ and $10^{8.3} M_\odot$.

As we aim at constraining the stellar mass content of haloes back to $z = 4$ we require high-quality observed SMFs at high redshift. In general wide high-redshift surveys capture many massive galaxies but are not deep enough to constrain the low-mass tail of the SMF. Conversely, deep surveys cover too small volumes to constrain the massive tail. In practice obtaining a SMF that is equally well constrained for massive and low-mass galaxies is difficult, as this would involve a survey that is both wide (capturing many massive galaxies) and deep (detecting even galaxies of very low mass).

We use the mass functions of the wide survey of Pérez-González et al. (2008) to constrain the massive end. These SMFs have been derived in 12 redshift bins from a sample of galaxies at $0 < z < 4$ selected in three different fields at $3.6 - 4.5$ $\mu m$ with the Infrared Array Camera (Fazio et al. 2004) on board the Spitzer Space Telescope (Werner et al. 2004). The survey covers a total area of 664 arcmin$^2$ and the obtained galaxy catalogue is 90 per cent complete down to $\sim 5$ $\mu$Jy at 3.6 $\mu m$ and $\sim 4$ $\mu$Jy at 4.5 $\mu m$. Due to the wide area of the survey, the SMFs put tight constraints on the abundances of massive galaxies up to $z = 4$, allowing for detailed modeling of the evolution of such galaxies.

For the low-mass end we use SMFs in 6 redshift bins by Santini et al. (2012), which have been obtained from Early Release Science observations taken in the $Y$, $J$, and $H$-bands with the near-IR Wide Field Camera 3 on board HST (Windhorst et al. 2011), and from deep $K$-band images taken with the near-IR VLT imager Hawk-I (Castellano et al. 2010). The galaxy catalogue has been selected in the $K$-band, covers an area of 33 arcmin$^2$, and is complete to a typical magnitude of $K = 25.5$. This very deep, albeit narrow, survey is able to resolve galaxies of low mass up to $z = 4.5$, and allows us to study the evolution of low-mass galaxies in detail. For all SMFs we have converted the stellar masses to agree with a Chabrier IMF. An overview of the 19 SMFs used in this work and their redshifts is shown in Figure 6.

## 3 CONNECTING GALAXIES AND HALOES

In this section we describe how we derive the relationship between the stellar mass of a galaxy and the mass of its dark matter halo. For this we first need to specify the SHM ratio. A direct comparison of the halo mass function and the stellar mass function shows that the baryons are converted into stars with very different efficiencies in haloes of different mass. Star formation is most efficient in systems like the Milky Way with $M_{\rm vir} \sim 10^{12} M_\odot$, and is substantially less efficient in much more massive or much less massive haloes. We adopt the parameterization of the SHM ratio of

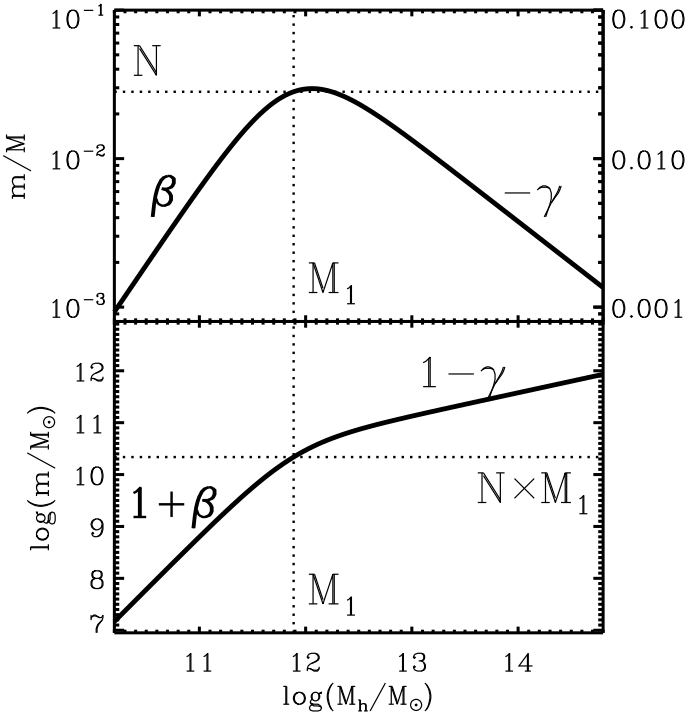


**Figure 1.** *Upper panel*: Sketch of the stellar-to-halo mass ratio as a function of halo mass peaking around the characteristic mass $M_1$ where it has the normalization $N$. It has a low-mass slope $\beta$ and a high mass slope $-\gamma$. *Lower panel*: Sketch of the stellar-to-halo mass relation as a function of halo mass. The low-mass slope is $1 + \beta$ and the high mass slope is $1 - \gamma$.

Moster et al. (2010):

$$\frac{m}{M} = 2\,N\,\left[\left(\frac{M}{M_1}\right)^{-\beta} + \left(\frac{M}{M_1}\right)^{\gamma}\right]^{-1}. \qquad (2)$$

It has four free parameters: the normalization of the SHM ratio $N$, a characteristic mass $M_1$, where the ratio is equal to the normalization $N$, and two slopes $\beta$ and $\gamma$ which indicate the behavior of $m/M$ at the low and high-mass ends, respectively. Figure 1 illustrates the SHM relation in two forms, indicating the four parameters. The halo mass where the SHM ratio is maximal is related to the characteristic mass $M_1$ by

$$M_{\rm max} = M_1 \left(\frac{\beta}{\gamma}\right)^{1/(\beta+\gamma)}. \qquad (3)$$

This SHM ratio can then be used to compute the average stellar mass in a dark matter halo. However, we expect that two haloes of the same mass $M$ may harbor galaxies with different stellar masses, since they can have different halo concentrations, spin parameters, and merger histories. Therefore we assume an intrinsic scatter around this average relation when assigning the stellar mass to an individual galaxy: we draw a stellar mass $m$ from a lognormal distribution with a mean value given by equation (2) and with a scatter of $\sigma_m(\log m) = 0.15$.

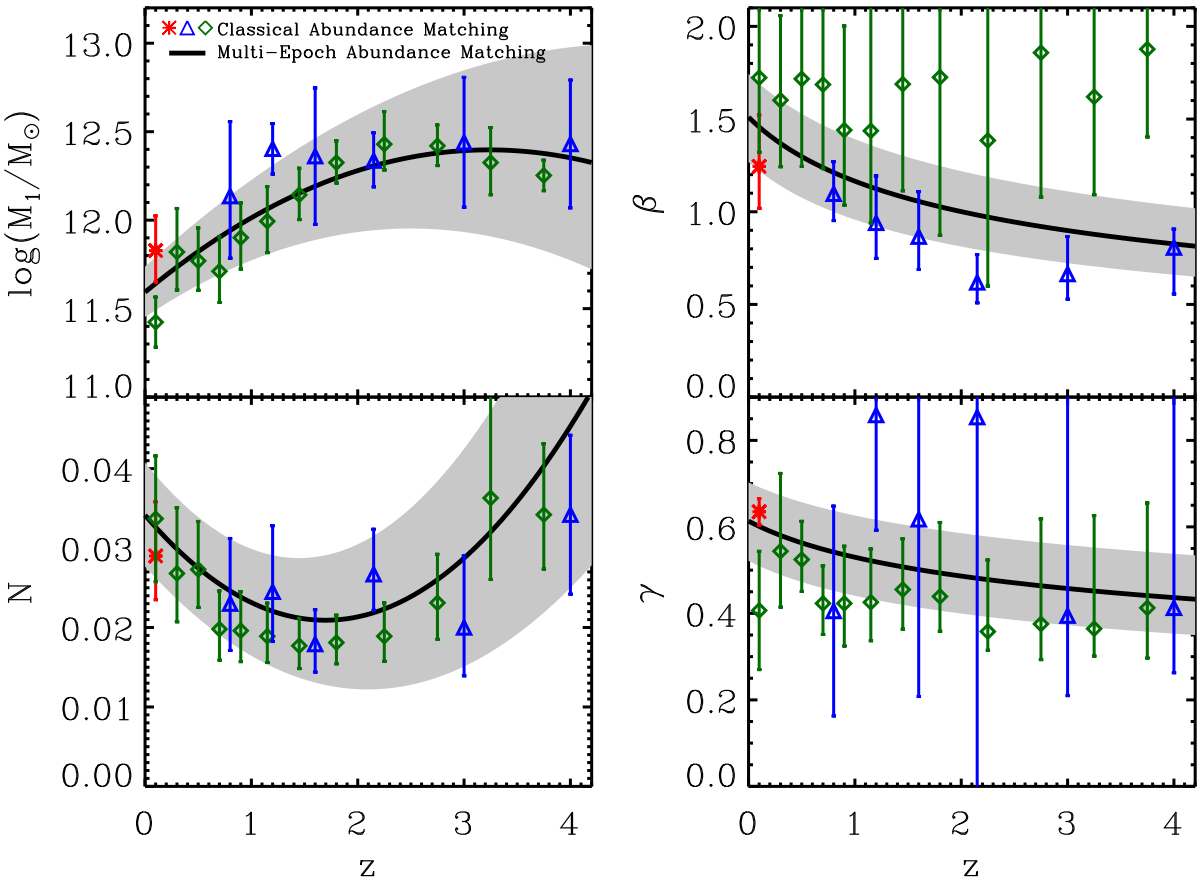


**Figure 2.** Evolution of the SHM relation parameters with redshift in a model without observational mass errors. The symbols correspond to the values that have been derived with the classical abundance matching approach at individual redshifts. Different colors represent the different SMFs that have been used to derive the SHM relation: red crosses for the SDSS SMF, green diamonds for the PG08 SMFs and blue triangles for the S12 SMFs. The solid line corresponds to a multi-epoch abundance matching model that takes into account that satellites are accreted at different epochs. The shaded area indicates the $1\sigma$ confidence levels. For $M_1$ and $N$ we assume a second order polynomial in $z$ and for $\beta$ and $\gamma$ a power law in $z$.

### 3.1 The evolution of the stellar-to-halo mass relation

As a first step, we investigate how the parameters of the SHM relation evolve with redshift. For this we assume that at a given redshift the relation between the stellar mass of a satellite galaxy and the maximum mass of its dark matter halo over its history is the same as the SHM relation of central galaxies. This assumption is only an approximation as the stellar mass of satellites is related to the halo mass at infall and the SHM relation is expected to have changed since this epoch. However, at any redshift the number of subhaloes of a given mass is lower than the number of main haloes of the same mass, so the approximation is not greatly in error. With this approach we are able study how the parameters of the SHM relation depend on redshift, and which functional form may be appropriate.

In order to constrain the parameters at a given redshift (where an observed SMF is available), we populate the haloes in the simulation with galaxies using the SHM relation to derive their stellar masses. Once the simulation box is filled with galaxies, it is straightforward to compute the model SMF. We then assign a likelihood to this model SMF by relating it to the observed SMF at this redshift:

$$\begin{aligned} \mathcal{L} &= \exp\left(-\chi_r^2\right) \\ \chi_r^2 &= \frac{1}{N_\Phi}\sum_{i=1}^{N_\Phi}\left(\frac{\log\Phi_{\rm mod}(m_i)-\log\Phi_{\rm obs}(m_i)}{\sigma_{\rm obs}(m_i)}\right)^2 . \end{aligned} \quad (4)$$

Employing a Markov chain Monte Carlo (MCMC) method, we sample the probability distribution for the parameters and extract the best-fit values and their $1\sigma$ errors. We repeat this procedure for every observed SMF available and plot the results in Figure 2 (symbols with errorbars).

The transition mass $M_1$ increases with increasing redshift and reaches a maximum around $z \sim 2$, after which it stays constant or even slightly decreases again. This means that at $z = 0$ the conversion of baryons into stars has been most efficient in haloes with a virial mass of $\log(M_{\rm vir}/M_\odot) \sim 11.7$, while at higher redshift the conversion was most efficient in more massive haloes with $\log(M_{\rm vir}/M_\odot) \sim 12.3$. The normalization $N$, i.e. the SHM ratio at the most efficient halo mass, decreases with increasing redshift, reaches a minimum around $z \sim 2$ and then increases again. We note that this does not imply that individual galaxies lose mass as halo mass generally increases for an individual system.

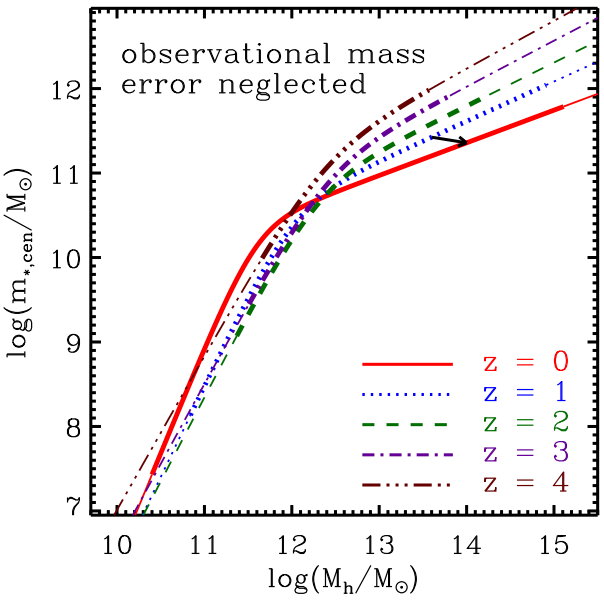


**Figure 3.** Stellar mass of the central galaxy as a function of the virial mass of the main halo for different redshifts for the model without observational mass errors. The thick lines correspond to the ranges where the relation is constrained by data, while the thin lines are extrapolations. The arrow shows the evolution of a system with $M_{\rm vir}(z=0) = 10^{14} M_\odot$ from $z = 1$ to 0, indicating that if observational mass errors are not accounted for, massive systems lose significantly more stellar mass than expected from stellar evolution models.

The low-mass slope $\beta$ is only constrained by the S12 SMFs. This is a consequence of the properties of the surveys from which the SMFs are obtained: The survey in PG08 does not provide strong constraints on the low-mass slope of the SMFs and consequently on $\beta$. The survey used in S12, on the other hand, is able to detect low-mass galaxies. From these constraints, we see that $\beta$ is decreasing with redshift, which means that the slope of the SHM relation becomes shallower with increasing redshift. For the high mass slope $\gamma$ constraints are provided only by the PG08 SMFs. These constraints indicate that $\gamma$ is also decreasing with redshift, i.e. the slope of the SHM relation becomes steeper with increasing redshift.

### 3.2 The multi-epoch abundance matching model

As we now have a first idea how the SHM parameters should evolve with redshift, we can construct a self-consistent model. As the next step in this multi-epoch abundance matching (MEAM) model, we determine a convenient redshift parameterization of the SHM parameters. For the characteristic mass $M_1$ and the normalization $N$, we use a second order polynomial in $z$, while for the slopes $\beta$ and $\gamma$ we use a power law:

$$\log M_1(z) = M_{10} + M_{11} z + M_{12} z^2, \quad (5)$$

$$N(z) = N_{10} + N_{11} z + N_{12} z^2, \quad (6)$$

$$\beta(z) = \beta_{10} (z+1)^{\beta_{11}}, \quad (7)$$

$$\gamma(z) = \gamma_{10} (z+1)^{\gamma_{11}}. \quad (8)$$

The stellar mass of a central galaxy is then given as a function of the virial mass of its dark matter halo $M_{\rm vir}$ and redshift $z$. For satellite galaxies, the stellar mass is now determined by employing the SHM relation at the time at which it still was a central galaxy, i.e. at the redshift of infall $z_{\rm inf}$. We then assume that the stellar mass of a satellite does not change after its subhalo entered the main halo, i.e. we neglect stellar stripping and star formation in the satellite. We thus get a redshift-dependent SHM relation $m(M, z)$ that depends on the virial mass of the main halo and redshift at the current epoch for central galaxies and on the infall mass of the subhalo and infall redshift for satellite galaxies. The stellar mass of a galaxy at redshift $z$ is then given by

$$m = \begin{cases} m(M_{\rm vir}, z) & \text{for host haloes} \\ m(M_{\rm inf}, z_{\rm inf}) & \text{for subhaloes .} \end{cases} \quad (9)$$

In this way we can derive the stellar mass of any galaxy just by employing the redshift-dependent SHM relation for central galaxies.

This relation can then be constrained with a set of SMFs at different redshifts. To this end we employ the simulation at all redshifts where an observed SMF is available and populate all main haloes and subhaloes in the simulation with galaxies using the redshift-dependent SHM relation to derive their stellar masses. We then compute the $N_z$ model SMFs for each redshift and assign a likelihood to the model by relating them to the corresponding observed SMFs:

$$\mathcal{L} = \exp\left(-\chi^2_{\rm r}\right)$$

$$\chi^2_{\rm r} = \frac{1}{N_z} \sum_{i=1}^{N_z} \chi^2_{z,i}$$

$$\chi^2_{z,i} = \frac{1}{N_{\Phi,i}} \sum_{j=1}^{N_{\Phi,i}} \left( \frac{\log \Phi_{\rm mod}(m_j) - \log \Phi_{\rm obs}(m_j)}{\sigma_{\rm obs}(m_j)} \right)^2 . \quad (10)$$

We again employ an MCMC method, sample the probability distribution for all the parameters and extract the best-fit values and their $1\sigma$ errors. We show the results in Figure 2 for the simultaneous fit to all SMFs (black line and shaded area). For all four SHM parameters, the lines for the simultaneous fit follow the trends that have been seen for the fits at individual redshifts.

The SHM relation for a set of redshifts between $z = 0$ and $z = 4$ is plotted in Figure 3. At a fixed halo mass at the high-mass end ($\log(M_{\rm vir}/M_\odot) \gtrsim 13.0$), the stellar mass increases with with increasing redshift. At intermediate halo masses ($\log(M_{\rm vir}/M_\odot) \sim 12.0$) the stellar mass decreases with increasing redshift, reaches a minimum at $z \sim 2$ and then increases again (reflecting the evolution of the normalization $N$). The fact that at a given halo mass the mass of the central galaxy is lower at present than at an earlier epoch does not necessarily imply that individual galaxies lose mass during their evolution, as haloes also become more massive over time. At a fixed halo mass of $\log(M_{\rm vir}/M_\odot) = 12.0$ the model stellar mass is $\log(m_*/M_\odot) = 10.5$ at $z = 4$ and only $\log(m_*/M_\odot) = 10.2$ at $z = 2$. However, a typical halo with $\log(M_{\rm vir}/M_\odot) = 12.0$ at $z = 4$ will increase its virial mass up to $\log(M_{\rm vir}/M_\odot) = 12.7$ at $z = 2$, for which the model stellar mass is $\log(m_*/M_\odot) = 11.0$, so that the stellar mass of the central galaxy does not decrease, but increase.

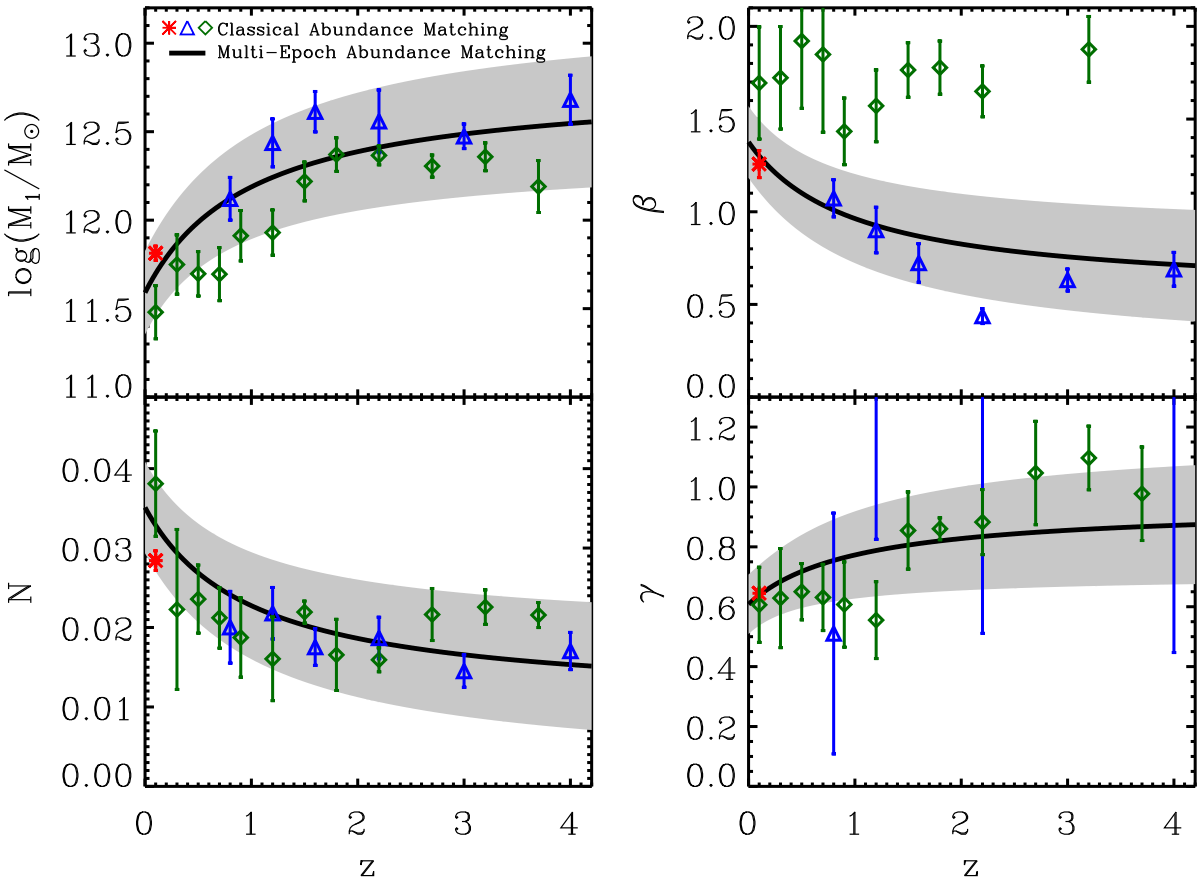


**Figure 4.** Evolution of the SHM relation parameters with redshift for the model including observational mass errors. The symbols of different color correspond to the classical abundance matching approach at individual redshifts: red crosses for the SDSS SMF, green diamonds for the PG08 SMFs and blue triangles for the S12 SMFs. The solid line corresponds to the multi-epoch abundance matching model. The shaded area indicates the $1\sigma$ confidence levels. For all four parameters we assume a linear dependence on the expansion factor $a = (1+z)^{-1}$.

However, we encounter a severe problem for massive galaxies at low redshift: the growth of halo mass cannot compensate for the decreasing stellar mass. A typical massive halo of $\log(M_{\rm vir}/M_\odot) = 14.0$ at $z = 0$ has grown from a $z = 1$ halo with a virial mass of $\log(M_{\rm vir}/M_\odot) = 13.6$. The model stellar mass for the central galaxy of this system at $z = 1$ is $\log(m_*/M_\odot) = 11.4$, while at $z = 0$ it is only $\log(m_*/M_\odot) = 11.3$. This would imply that massive systems lose stellar mass at low redshift and is unphysical, as stellar mass loss rates from supernovae are much lower than accretion rates onto the central galaxy. This indicates that an important effect has been neglected in our model and that the effects of this missing ingredient are most severe at the massive end. In the following section we show that neglecting errors in the observed stellar mass impacts the results for massive galaxies strongly and that taking this into account results in a model where galaxies do not lose stellar mass during their evolution.

### 3.3 Introducing observational mass errors in the model

Estimating stellar masses for an observed sample of galaxies involves obtaining the luminosities of the galaxies and then converting these to stellar masses through a stellar population synthesis model and dust corrections. The errors introduced in all these steps are typically of the order of the uncertainties in the stellar populations synthesis analysis. Assuming that these errors are Gaussian, the shape of the SMF implies that at a given observed mass there are more galaxies with a lower true mass than galaxies with a higher true mass, i.e. more galaxies are scattered in than scattered out. As a result the observed SMF is shallower than the true SMF, particularly at the massive end. It is important to include this effect in our model.

We do this by adding a Gaussian scatter to the stellar mass of each model galaxy. An 'observed' stellar mass in our model is thus obtained in three steps: We first compute the average mass for a given halo mass and redshift (or infall halo mass and infall redshift for subhaloes), then we add a fixed intrinsic scatter of $\sigma_m(\log m) = 0.15$ dex to account for different halo parameters and histories, and finally we add an observational scatter to account for errors in the obser-

**Table 1.** Fitting results for the redshift-dependent stellar-to-halo mass relationship.

| | $M_{10}$ | $M_{11}$ | $N_{10}$ | $N_{11}$ | $\beta_{10}$ | $\beta_{11}$ | $\gamma_{10}$ | $\gamma_{11}$ |
|---|---|---|---|---|---|---|---|---|
| Best fit | 11.590 | 1.195 | 0.0351 | -0.0247 | 1.376 | -0.826 | 0.608 | 0.329 |
| $\sigma$ | 0.236 | 0.353 | 0.0058 | 0.0069 | 0.153 | 0.225 | 0.059 | 0.173 |

**Notes:** All masses are in units of $M_\odot$ .

vational estimate of stellar mass. The value of this scatter is $\sigma_{\rm obs} = 0.1$ dex for the SDSS SMF (as estimated by LW09), $\sigma_{\rm obs} = 0.3$ dex for the SMFs by PG08 and S12 at $z < 3$ and $\sigma_{\rm obs} = 0.45$ dex for the SMFs at $z \geqslant 3$ (see appendix B of PG08).

### *3.3.1 The evolution of the SHM parameters*

First we employ the classical abundance matching approach as described in Section 3.1, now taking into account observational mass errors, to investigate how the SHM parameters evolve with redshift, and if a different functional form has to be adopted. The results are plotted in Figure 4 (symbols with errorbars). As for the fit without observational mass errors, the transition mass $M_1$ increases with increasing redshift. This increase is strong at low redshift, while at high redshift $M_1$ increases only slightly. Unlike before we do not find that $M_1$ has a maximum beyond which it decreases again. This result implies that at high redshift, massive haloes with $\log(M_{\rm vir}/M_\odot) \sim 12.5$ are most efficient in converting baryons into stars, while at lower redshift the halo mass for which the baryon conversion efficiency is maximal, decreases towards $\log(M_{\rm vir}/M_\odot) \sim 11.6$.

The normalization $N$ (the conversion efficiency at the peak) is now found to decrease monotonically with redshift. The reason why the normalization does not change much at low redshift with respect to the model without observational scatter, but is very different at high redshift, is the evolution of the low-mass slope $\alpha$ of the SMF. At low redshift this slope is very shallow, so relatively few galaxies are scattered from lower masses towards the characteristic mass of the SMF (which corresponds to the peak efficiency). At high redshift, the low-mass slope is much steeper, so that more galaxies are scattered towards (and beyond) the mass of the peak efficiency. As a result, the observed SMFs at low redshift are very similar to the true SMFs, while at high redshift the observed SMFs are shifted towards higher masses. Therefore it appears as if the normalization is increasing at high redshift, if the observational mass error is not taken into account. When we account for this, we find that the true SMFs are shifted to lower masses and the normalization of the SHM ratio $N$ no longer increases at high redshift.

The results for the low-mass slope $\beta$ are very similar to what we found before. This is a consequence of the shallow low-mass slope of the SMFs, so that the observational mass error does not change the SMFs much. As before, $\beta$ is decreasing with increasing redshift, so that the slope of the SHM relation becomes shallower with increasing redshift. Again, $\beta$ is only constrained by the S12 SMFs.

The high-mass slope $\gamma$ is very different to what was found without observational mass errors. Where before $\gamma$ was decreasing with increasing redshift, we now find that $\gamma$ is increasing. The reason for this is the steep slope of the SMFs at the massive end, which means that the true SMFs are even steeper than the observed SMFs. Therefore the high mass slope of the SHM relation has to become shallower which yields a larger $\gamma$. Here, the constraints are provided only by the PG08 SMFs, as only this survey is wide enough to detect very massive galaxies.

### *3.3.2 The multi-epoch abundance matching model including observational mass errors*

Now that we have checked how the SHM parameters evolve with redshift, we can again employ our self-consistent model. As this evolution is found to be different with respect to the model without observational mass errors, we first need to determine the new redshift parameterization of the SHM parameters. As all parameters evolve considerably at low redshift, but evolve only slightly at high redshift, we found it more convenient to use a linear dependence on the expansion parameter $a = (z+1)^{-1}$:

$$\log M_1(z) = M_{10} + M_{11}(1-a) = M_{10} + M_{11}\frac{z}{z+1}, \quad (11)$$

$$N(z) = N_{10} + N_{11}(1-a) = N_{10} + N_{11}\frac{z}{z+1}, \quad (12)$$

$$\beta(z) = \beta_{10} + \beta_{11}(1-a) = \beta_{10} + \beta_{11}\frac{z}{z+1}, \quad (13)$$

$$\gamma(z) = \gamma_{10} + \gamma_{11}(1-a) = \gamma_{10} + \gamma_{11}\frac{z}{z+1}. \quad (14)$$

The stellar mass is given by equation (2) as a function of the virial mass of the main halo $M_{\rm vir}$ and redshift $z$ for central galaxies and as a function of the infall mass of the subhalo $M_{\rm inf}$ and infall redshift $z_{\rm inf}$ for satellite galaxies (see equation (9)). We constrain the eight parameters $M_{10}$, $M_{11}$, $N_{10}$, $N_{11}$, $\beta_{10}$, $\beta_{11}$, $\gamma_{10}$ and $\gamma_{11}$ by fitting our model to a set of SMFs at different redshifts. Again we employ the simulation at those redshifts where an observed SMF is available and populate all main haloes and subhaloes in the simulation with galaxies using the redshift-dependent SHM relation to derive their stellar masses. We then compute the 19 model SMFs and employ an MCMC method to find the best-fit values and their $1\sigma$ errors. The results are summarized in Table 1.

We show the results in Figure 4 for the simultaneous fit to all SMFs (black line and shaded area). The redshift evolution of all four SHM parameters in the simultaneous fit follow the trends that have been seen for the fits at individual redshifts. We plot the SHM relation and the baryon conversion efficiency for a set of redshifts between $z = 0$ and $z = 4$ in Figure 5. At a fixed halo mass, the stellar mass now decreases with increasing redshift for low mass, intermediate

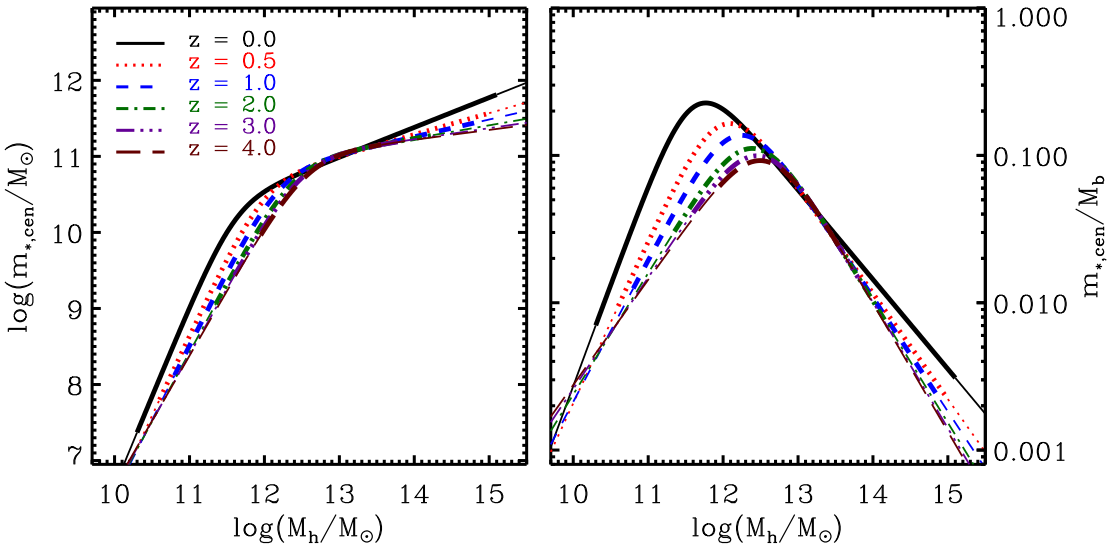


**Figure 5.** Stellar-to-Halo mass relation for central galaxies as a function of redshift. This relation is also valid for satellite galaxies when virial mass and current redshift are substituted with subhalo infall mass and infall redshift, so that the satellite stellar mass is obtained when it was last a central galaxy and does not change until it is accreted onto the central galaxy. *Left panel:* Evolution of the SHM relation. *Right panel:* Evolution of the baryon conversion efficiency $m_{*,\rm cen}/M_b = m_{*,\rm cen}/(M_{\rm vir} f_b) = (m_{*,\rm cen}/M_{\rm vir}) \times (\Omega_m/\Omega_b)$. The thick lines correspond to the ranges where the relation is constrained by data, while the thin lines are extrapolations.

and massive galaxies. As a consequence, all central galaxies grow with time. Moreover, independent of halo mass, we find that in all systems the central galaxies grow faster in stellar mass than the respective main haloes accrete dark matter.

Finally we compare our model SMFs to the observed ones in Figure 6. The model SMFs have been computed using the result of the simultaneous fit to all SMFs, i.e. the parameters given in Table 1. The dashed lines show the 'true' SMFs, that have been computed after intrinsic scatter has been added to the galaxy catalogue, but before observational mass error. The solid lines show the model SMFs, after mass errors have been included. At low redshift and at low stellar masses, the observational mass errors do not impact the shape of the SMFs significantly, as the slope of the SMF is shallower than at higher redshift and at the massive end. Beyond the characteristic stellar mass, the 'true' SMFs are much steeper than the observed ones, so that there are substantially fewer very massive galaxies at high redshift than the observational SMFs appear to indicate.

The model SMFs including observational mass error are in very good agreement with the observed SMFs. This indicates, that our parameterization of the redshift evolution of the SHM relation is compatible with observational constraints. However, there are a number of discrepancies, that stem mainly from the fact that the observed SMFs of different authors are not in agreement. The SMF of PG08 at low redshift ($z = 0.1$) is higher than our model, while the SDSS SMF is fit very well. The reason for this is that the SDSS has much smaller errors than the PG08 SMF, so that during the fit a much higher likelihood is given to the model that agrees with the SDSS. At higher redshift there are discrepancies between the model and the observed SMFs at the low-mass end. While the model overpredicts the abundance of low-mass galaxies with respect to the PG08 SMFs, it underpredicts the abundance with respect to the S12 SMFs. This is due to the PG08 SMFs having a much shallower slope than the S12 SMFs. As the errors on both sets of observations are of the same order, a model is favored that yields average abundances.

## 4 THE EVOLUTION OF THE STELLAR CONTENT

Having constrained the evolution of the SHM relation for central galaxies, we can now use our model to infer the evolution of the stellar content of galaxies. To this end we employ the dark matter halo merger trees that have been extracted from the *MS* and *MS-II*. These merger trees connect haloes at any given epoch to their descendants at later epochs or to their progenitors at earlier epochs. As our redshift-dependent SHM relation determines the connection between galaxies and haloes at any epoch, we can use the connection between haloes across time to infer the connection between galaxies across time. By averaging over a sample of haloes with the same mass at $z = 0$, our model yields the average stellar mass growth of central galaxies as a function of halo mass. We apply this method for sets of halo masses between $10^{11} M_\odot$ and $10^{14} M_\odot$. This analysis is related to previous studies that employed semi-analytic models (De Lucia et al. 2006; De Lucia & Blaizot 2007; Guo & White 2008). For a comparison and discussion we refer to Section 5.

As a first step, we select a sample of merger trees by fixing the virial mass of the main halo at $z = 0$. In the next step, we populate the haloes in these merger trees using our redshift-dependent SHM relation to compute the stellar masses of their central galaxies. At every epoch, i.e. simulation snapshot, we then compute the average stellar mass of the central galaxies in the main haloes. Finally, we calculate the difference of the average central galaxy stellar mass between two subsequent snapshots and divide this by the time that has elapsed between those snapshots to derive the

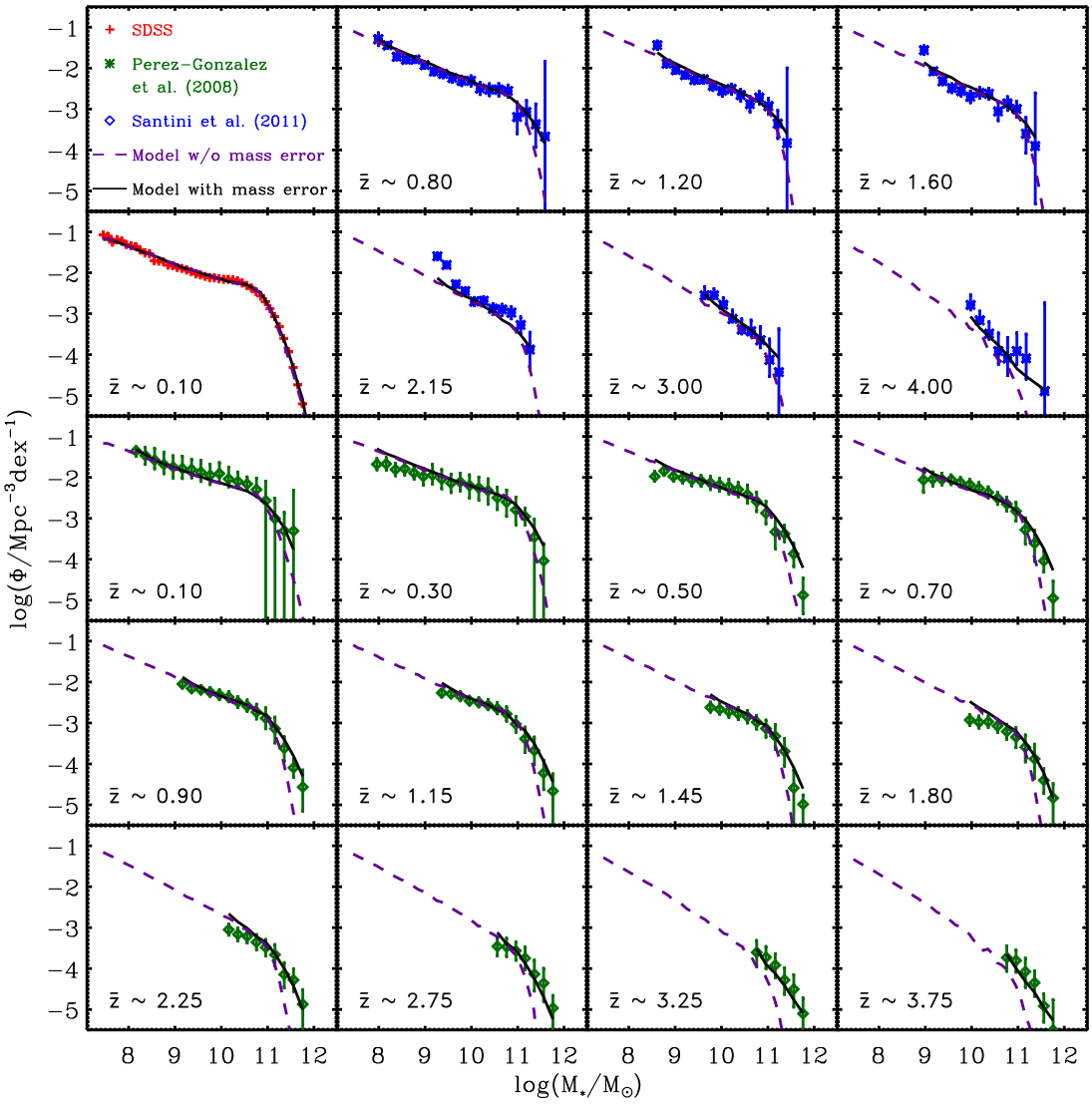


**Figure 6.** Comparison of the model (lines) and the observed SMFs (symbols). The redshift is indicated in each panel. The model SMFs have been computed using the results of the fit including observational mass error. The solid lines show the SMFs when mass errors are included and represent a fit to the observations. The dashed lines show the 'true' SMFs, before observational mass error is added.

average stellar mass growth rate of the central galaxies. By doing this for a set of trees in halo mass bins, we can compute the average growth rate as a function of the $z = 0$ halo mass and redshift.

In the left panels of Figure 7 we show the average fraction of $z = 0$ mass assembled as a function of redshift for dark matter haloes and central galaxies. For four $z = 0$ halo masses, the assembly history of a central galaxy is compared to that of its parent halo. In low-mass systems with $\log(M_{\rm vir}/M_\odot) \lesssim 12.5$ the halo grows much slower than its central galaxy. This indicates that in these systems the growth is dominated by internal gas physical processes such as cooling and star formation. Only rather little external material is falling into the halo. For massive systems with $\log(M_{\rm vir}/M_\odot) \gtrsim 12.5$ the trends are opposite at low redshift: the fractional growth of haloes since $z \sim 2$ is much stronger than the stellar growth of their central galaxy. A large fraction of the stellar mass of massive galaxies is already in place at $z \lesssim 2$. In these massive systems the growth is dominated by external processes at late times, as they are accreting large amounts of material. While the halo grows rapidly, the central galaxy does not, as most of the accreted systems take a very long time to reach the centre of the halo and instead survive to $z = 0$ as 'satellite' members of the group or cluster.

To further study when most of the stellar and halo mass was in place we follow and extend the analysis by Conroy & Wechsler (2009). We plot the average assembly redshift of main haloes and central galaxies as a function of $z = 0$ mass in the right panel of Figure 7. We show the redshift at which 25, 50, and 75 per cent of the present stellar and halo mass was already in place. In low-mass systems, the stellar mass assembled much later than the halo mass. For a system with $M_{\rm vir} = 10^{12} M_\odot$, half of the stellar mass

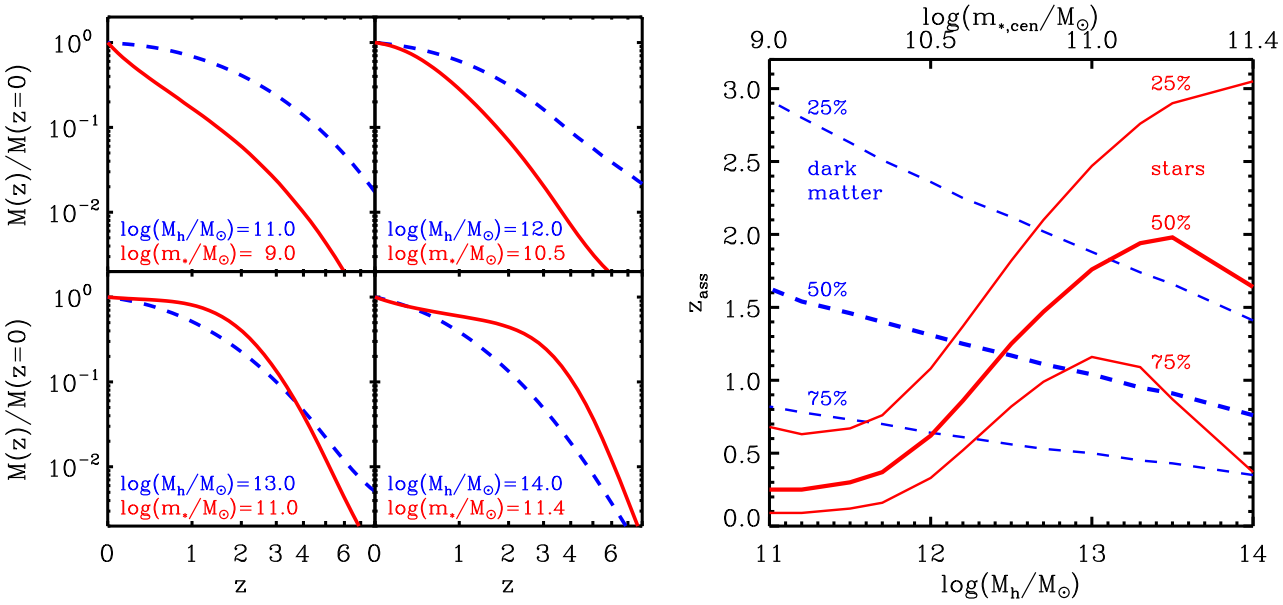


**Figure 7.** *Left panels:* Average fraction of $z = 0$ mass assembled as a function of redshift for dark matter haloes (blue dashed lines) and central galaxies (red solid lines). Each panel compares the mass assembly history of a central galaxy to that of its parent halo. The $z = 0$ halo and stellar masses are indicated in each panel. While for low-mass dark matter haloes most of the mass assembles at early times, massive haloes only assemble late. For galaxies these trends are opposite. *Right panel:* Average formation redshift of dark matter haloes (blue dashed lines) and central galaxies (red solid lines) as a function of $z = 0$ mass. The three different lines indicate the redshift at which 25, 50, and 75 per cent of the mass was in place.

of the central galaxy forms after redshift $z = 0.7$ while half of the virial mass was already assembled by redshift $z = 1.3$. In more massive systems haloes assemble later while galaxies assemble earlier: for a system with a $z = 0$ halo mass of $M_{\rm vir} = 10^{13} M_\odot$, half of the halo has assembled only by redshift $z = 1.0$, but half of the stellar mass was already in place by redshift $z = 1.8$.

Very massive galaxies in haloes with $M_{\rm vir} = 10^{14} M_\odot$ show a very interesting behavior: while they begin to form very early and have 25 per cent of their stellar mass in place already by redshift $z = 3.0$, it takes them a long time to fully assemble. Half of their stellar mass is in place only by redshift $z = 1.6$, while 75 per cent is assembled by $z = 0.3$. The final $z = 0$ stellar mass is then assembled very quickly. The reason why these massive galaxies grow very fast at early times, only grow slowly at intermediate redshifts and grow fast again at late times can be found in the two processes that contribute to the growth of galaxies. At high redshift, a massive galaxy grows effectively by star formation, while at low redshift, stellar accretion leads to a fast growth. At intermediate redshift however, neither of these processes is effective, so that the galaxy grows only very slowly. In the following section we aim to constrain and separate these two processes. Note that while massive galaxies assemble their final stellar mass only late, the stars in these galaxies have formed much earlier, such that this result is not in conflict with the observation that the stars in massive systems are older than stars in low-mass galaxies.

### 4.1 Star formation and accretion histories

The stellar mass of a galaxy can grow either by star formation inside the galaxy (in-situ) or by the assembly of stars that formed outside the galaxy and have been accreted later (ex-situ). In principle, both processes can contribute simultaneously to the growth of a central galaxy, but in practice one process will dominate over the other as a function of halo mass and redshift. In order to separate the contributions from star formation and accretion, we have first to determine the amount of accretion of subhaloes onto the central object in the halo. Using our model, we can then populate these subhaloes with satellite galaxies and compute the stellar accretion rate. Finally, the SFR can be determined from the difference between the total growth rate and the accretion rate.

We use the same set of dark matter halo merger trees as before, i.e. we use all trees with a common $z = 0$ virial mass of the main halo and assign a stellar mass to all haloes and subhaloes using our redshift-dependent SHM relation. For every simulation snapshot, we then record all satellite galaxies that are accreted onto the central galaxy until the time of the next snapshot. We note, that, by construction, this also includes orphan galaxies. At each snapshot we then sum the stellar mass of all recorded merging galaxies and divide this by the number of central galaxies in the sample (which corresponds to the number of merger trees). We further assume that a fraction of satellite stars $f_{\rm esc} = 0.2$ escapes from the central galaxy and ends up in the halo as diffuse stellar material not detected in standard surveys. This fiducial value is motivated by high-resolution simulations of binary galaxy mergers (e.g. Nipoti et al. 2003; Naab & Burkert 2003; Moster et al. 2011). For a different value the resulting stellar accretion and star formation rates change accordingly (e.g. for $f_{\rm esc} = 0$ the accretion rates are 25 per cent higher). In this way we get the average stellar

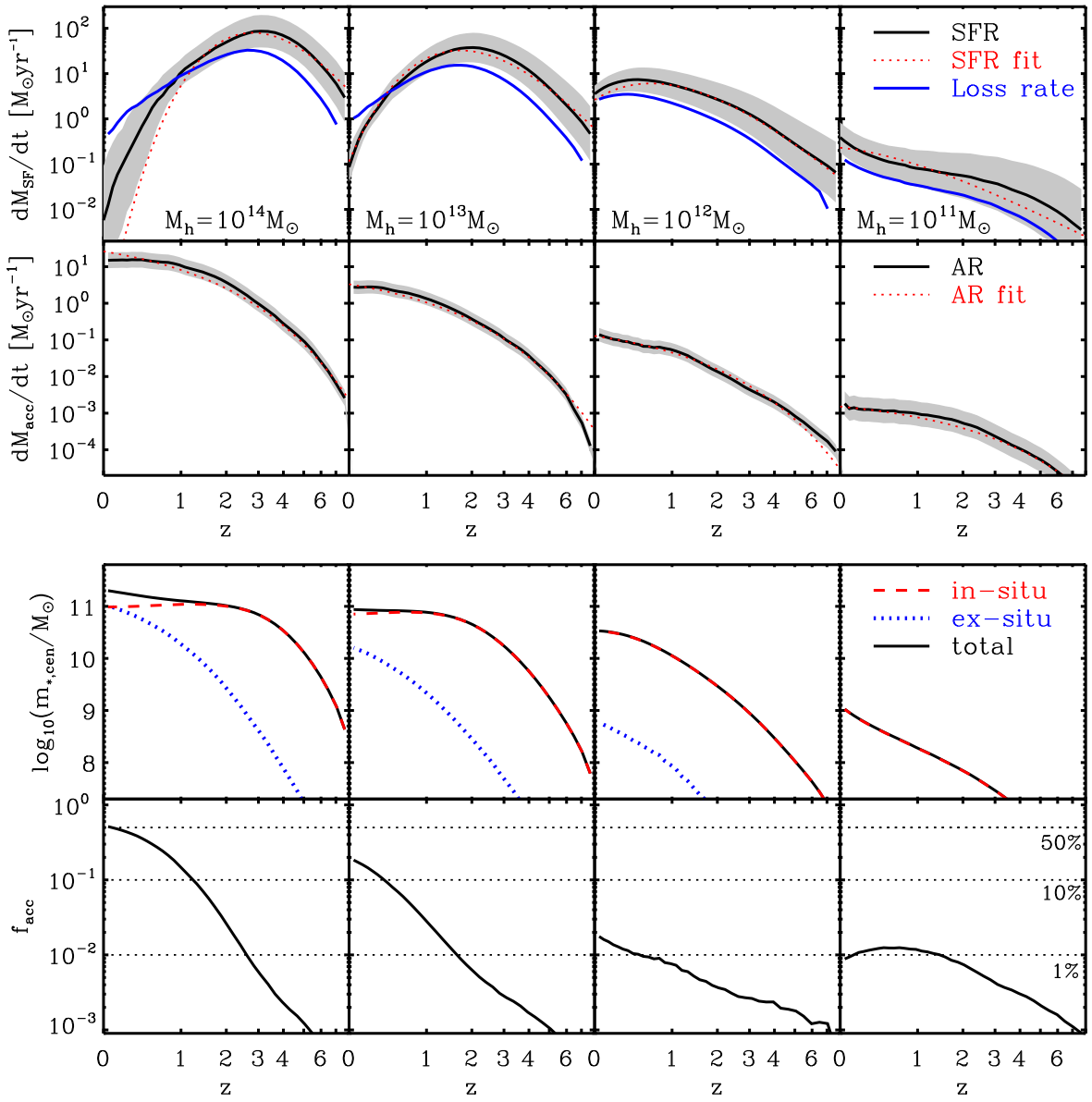


**Figure 8.** Star formation and accretion histories for different $z = 0$ halo masses. The rows from top to bottom show the star formation history, the stellar accretion history, the stellar mass formed in-situ and ex-situ, and the fraction of ex-situ formed stars. Each column represents a different $z = 0$ halo mass. In the first two rows the black lines and shaded areas represent the rates that have been derived with our model and their $1\sigma$ confidence levels. The red lines are fits to these relation as given by equations (17)-(20) and (21)-(23). The blue line in the first row shows the stellar mass loss rate. In the third row, the red dotted lines give the stellar mass of in-situ formed stars that have survived, the blue dashed lines give the stellar mass that has formed ex-situ, and the black line is the total stellar mass in the central galaxy. The dotted lines in the fourth row indicate that 50, 10 and 1 per cent of the stellar mass has formed ex-situ.

accretion rate onto the central galaxy as a function of the $z = 0$ halo mass and redshift.

Having determined the total stellar growth rate and the amount of growth that is due to accretion, the SFR of an average galaxy can be computed from the residual stellar mass growth attributed to star formation. However, the relation between this residual growth rate and the SFR is complicated by mass loss due to dying stars:

$$\frac{\mathrm{d}m_{\rm res}}{\mathrm{d}t} = \frac{\mathrm{d}m_{\rm tot}}{\mathrm{d}t} - \frac{\mathrm{d}m_{\rm acc}}{\mathrm{d}t} = \frac{\mathrm{d}m_{\rm SF}}{\mathrm{d}t} - \frac{\mathrm{d}m_{\rm loss}}{\mathrm{d}t} = \frac{\mathrm{d}m_{\rm IS}}{\mathrm{d}t} \,. \quad (15)$$

This equation states that the residual growth rate $\mathrm{d}m_{\rm res}/\mathrm{d}t$, which is defined as the difference between the total growth rate $\mathrm{d}m_{\rm tot}/\mathrm{d}t$ and the accretion rate $\mathrm{d}m_{\rm acc}/\mathrm{d}t$, is given by the difference between the SFR $\mathrm{d}m_{\rm SF}/\mathrm{d}t$ and the stellar mass loss rate $\mathrm{d}m_{\rm loss}/\mathrm{d}t$, and corresponds to a net in-situ growth rate $\mathrm{d}m_{\rm IS}/\mathrm{d}t$. It can be solved iteratively, starting with a SFR that is equal to the residual growth rate at every epoch. We go to the time of the first snapshot and compute the amount of stellar mass that is formed in an average galaxy. Then we move to the second snapshot and compute both the stellar mass that forms at this time and the stellar mass that is lost in the population that formed in the first

snapshot. For the latter we employ the formula

$$f_{\rm loss}(t) = 0.05 \times \ln\left(\frac{t + 3\times10^5 \text{ yr}}{3\times10^5 \text{ yr}}\right) , \qquad (16)$$

where $f_{\rm loss}(t)$ is the fraction of mass lost by a stellar population with an age $t$. This formula is a fit to the mass loss of a stellar population with a Chabrier (2003) IMF as developed by Bruzual & Charlot (2003) and implies that 40 per cent of stellar mass is lost within 1 Gyr and 50 per cent of stellar mass is lost within 10 Gyr.

We then move to the third snapshot, compute the stellar mass that forms at this time and derive the stellar mass that is lost in the populations that formed in the first and second snapshots. This procedure is continued until $z = 0$, while at every snapshot the amount of lost stellar mass is the sum of the lost mass of all populations that have formed until then. We can then compute the loss rate between subsequent snapshots and the in-situ growth rate as the difference between SFR and loss rate. This in-situ growth rate is then compared to the residual growth rate as described by equation 15. The difference between those rates is then added to the SFR (separately at each snapshot) and the procedure is repeated and iterated until the in-situ growth rate and the residual growth rate are equal. We repeat this procedure for each sample of halo merger trees with a given $z = 0$ halo mass.

The resulting SFRs and accretion rates are shown in the first and second rows of Figure 8 (black solid lines), respectively, for four different $z = 0$ halo masses. The $1\sigma$ confidence levels for both rates (shaded areas) have been computed by employing the upper and lower estimates for mean stellar masses according to our SHM relation. We have also added the stellar mass loss rates in upper panels (blue line). All results represent the average rates, i.e. the average of both red and blue galaxies at a given $z = 0$ halo mass. Of course, individual galaxies can have higher or lower SFRs depending on other galaxy properties like color, so that blue (red) galaxies can have higher (lower) SFRs.

We find that the star formation history of central galaxies peaks at a certain redshift. This peak SFR redshift depends on halo mass: for massive systems this peak occurs at high redshift ($z = 3$ for $M_{\rm vir} = 10^{14} M_\odot$) while for lower masses the SFR peaks at a lower redshift ($z = 0.5$ for $M_{\rm vir} = 10^{12} M_\odot$). For systems with an even lower mass of $M_{\rm vir} \lesssim 10^{11.7} M_\odot$ the peak has not been reached yet by $z = 0$. After the peak has been reached, the SFR quickly drops, such that massive galaxies are quenched at $z \sim 2$. Furthermore, the peak SFR is higher in more massive systems. We also find that in systems that are more massive than $M_{\rm vir} = 10^{12.5} M_\odot$, the stellar mass loss rate due to dying stars is larger than the SFR at $z = 0$, such that the mass of stars present in the central galaxy is decreasing.

The accretion rates increase with time for all systems. Massive systems have a high accretion rate that dominates the total growth rate at late times, while for low-mass systems, accretion is insignificant at all times. For a system with $M_{\rm vir} = 10^{14} M_\odot$ the accretion rate dominates over the SFR at $z < 1$. The halo mass at which the accretion rate and the SFR are equal at $z = 0$ is $M_{\rm vir} = 10^{12.7} M_\odot$. For lower masses the contribution of accretion to the total growth rate quickly drops. The reason why accretion contributes significantly to the overall growth in massive systems and it is insignificant in low-mass systems can be inferred from the SHM relation. Massive haloes host relatively massive subhaloes, and these subhaloes are filled with relatively massive satellite galaxies. The subhaloes that have e.g. one tenth of the main halo mass host galaxies that are almost as massive as the central galaxy, so that the resulting accretion rates are high. In low-mass systems, however, the subhaloes are almost entirely devoid of stars, so that the accretion of the subhaloes onto the center does not result in a significant stellar accretion rate. Moreover, Figure 7 shows that low-mass haloes have largely assembled by $z = 1$, so that any late time growth has to come from star formation.

To compare further the relative importance of star formation and accretion for systems of different mass, we plot in the third row of Figure 8 the amount of stellar mass that has formed in-situ, i.e. through star formation, and the amount that has formed ex-situ, i.e. has been accreted. In the fourth row we show the fraction of stellar mass of the central galaxy that has formed ex-situ. In massive systems with $M_{\rm vir} \geqslant 10^{13} M_\odot$, all of the stars that have formed in-situ and survived were already in place at high redshift ($z \gtrsim 2$). Although, the loss rate is higher than the accretion rate at late times, and the amount of in-situ stellar mass has decreased since $z \sim 2$, the total stellar mass of the system increases with time, as the accretion rate compensates for the lost stellar mass. In very massive systems with $M_{\rm vir} = 10^{14} M_\odot$ more than half of the central stellar mass is formed ex-situ. In lower mass systems the amount of ex-situ stellar mass is decreasing considerably: for $M_{\rm vir} = 10^{13} M_\odot$ the fraction of ex-situ stars is 20 per cent, for $M_{\rm vir} = 10^{12} M_\odot$ the fraction is 2 per cent, and for $M_{\rm vir} = 10^{12} M_\odot$ the fraction is 1 per cent. At high redshift ($z \gtrsim 2$), the amount of stellar mass that has formed ex-situ is negligible for systems of all masses. We further note that the accretion rates grow more rapidly in massive systems than in systems of low mass.

The connection between star formation and accretion history and the virial mass of the system can be of general use in constraining models of cooling, star formation and feedback in galaxies. These relations have been derived entirely from observations with an empirical model. Although this model makes no reference to the physical processes that drive the evolution of galaxies, it can be very helpful in order to constrain more physical models. In order to easily compare our model predictions to the results of other models such as simulations and semi-analytic models, we provide simple fitting functions to the star formation and accretion histories.

We find that at a given $z = 0$ main halo mass the SFR is well fit by the relation:

$$\begin{aligned} \frac{{\rm d}m_{\rm SF}}{{\rm d}t}(z) &= f_1\, a^{f_2}\, \exp\left(\frac{f_2}{f_3}\,(1.0 - a)\right) \\ &= f_1\,(1+z)^{-f_2} \exp\left(\frac{f_2}{f_3}\frac{z}{1+z}\right). \end{aligned} \qquad (17)$$

The parameters $f_1$, $f_2$, and $f_3$ depend on the $z = 0$ halo

mass of the system and follow the relations:

$$f_1 = f_{10}\ \exp\left(-\frac{(\log(M_{\rm vir}/M_\odot)-f_{11})^2}{2\,f_{12}^2}\right)\ , \quad (18)$$

$$f_2 = f_{20}+f_{21}\ \log\left(\frac{M_{\rm vir}}{10^{12}M_\odot}\right)\ , \quad (19)$$

$$\log(f_3) = f_{30}+f_{31}\left(\frac{M_{\rm vir}}{10^{12}M_\odot}\right)^{f_{32}}\ . \quad (20)$$

The parameter $f_1$ can be interpreted as the SFR at $z = 0$, $f_2$ is the slope of the star formation history at high redshift, and $f_3$ corresponds to the expansion factor $a$ of the peak SFR. The values of the fitting parameters are:

$f_{10} = 2.658\ M_\odot\ {\rm yr}^{-1}$, $f_{11} = 11.937$, $f_{12} = 0.424$,
$f_{20} = 5.507$, $f_{21} = 2.437$,
$f_{30} = -0.915$, $f_{31} = 0.696$, $f_{32} = -0.159$ .

The SFRs obtained with this fitting function are compared to the inferred ones in Figure 8 (red lines). Overall the global fit is very close to the model predictions. For very massive galaxies with $M_{\rm vir} = 10^{14}M_\odot$ at low redshift ($z < 1$), the fitting function is lower than the model SFR, although it is still within the $1\sigma$ confidence levels.

The accretion history for systems of a given $z = 0$ main halo mass can be described with an exponential dependence on redshift:

$$\frac{{\rm d}m_{\rm acc}}{{\rm d}t}(z) = g_1\ \exp\left(-\frac{z}{g_2}\right)\ . \quad (21)$$

The parameters $g_1$, and $g_2$ are functions of the $z = 0$ halo mass of the system and are given by:

$$g_1 = g_{10}\left[\left(\frac{M_{\rm vir}}{10^{12.5}M_\odot}\right)^{g_{11}}+\left(\frac{M_{\rm vir}}{10^{12.5}M_\odot}\right)^{g_{12}}\right]^{-1}\ , \quad (22)$$

$$g_2 = g_{20}+g_{21}\left(\frac{M_{\rm vir}}{10^{12}M_\odot}\right)^{g_{22}}\ . \quad (23)$$

The parameter $g_1$ gives the stellar accretion rate at $z = 0$, and $g_2$ is the slope of the accretion history. The values of the fitting parameters are:

$g_{10} = 1.633\ M_\odot\ {\rm yr}^{-1}$, $g_{11} = -2.017$, $g_{12} = -0.806$,
$g_{20} = 0.855$, $g_{21} = 0.098$, $g_{22} = -0.797$ .

The accretion rates obtained with this fitting function are compared to the inferred ones in Figure 8 (red lines). The global fit is very close to the model prdictions for all redshifts and halo masses.

### 4.2 Cosmic star formation rate density

In order to check whether our model SFRs are in agreement with observational constraints, we compare our model prediction for the evolution of the cosmic SFR density to data in the literature. For this we compute the SFR for each halo in the simulations using our recipe as given by equations (17)-(20) and compute the volume density for each snapshot. We compare the result to observational estimates derived with different methods in Figure 9. This comparison includes estimates derived from the UV (Salim et al. 2007; van der Burg et al. 2010; Bouwens et al. 2009; Robotham & Driver 2011; Bouwens et al. 2011; Cucciati et al. 2012), H$\alpha$ (Ly et al. 2011), both UV and IR (Zheng et al. 2007), the FIR (Rujopakarn et al. 2010) and from radio observations (Smolčić et al. 2009; Dunne et al. 2009; Karim et al. 2011).

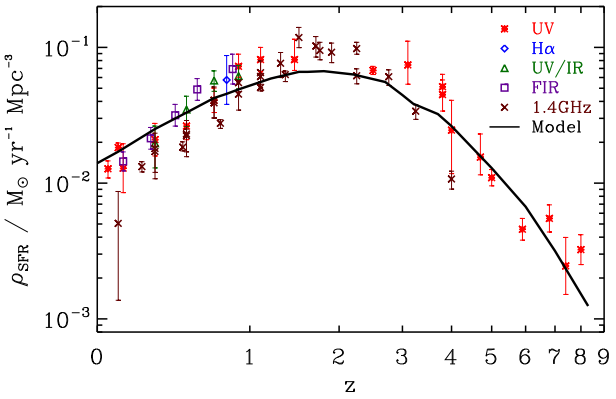


**Figure 9.** Star formation rate density as a function of redshift. The symbols of different colors give observational estimates derived with different methods. The black line is the result of our model. The model was constrained with observed SMFs at different redshifts and has not been fit to observed SFRs. Still the model is in excellent agreement with the data.

Our model is in excellent agreement with the data at all redshifts. We note that our model was only constrained with observed SMFs at different redshifts and has not been fit to observed SFRs. This means that the observed SMFs are broadly consistent with observational inferences for SFRs once observational mass errors are taken into account. Moreover, this shows that our choice for the parameterization for the redshift-dependent SHM relation is consistent with observational constraints, and that our inferred recipe for the mass-dependent star formation histories gives reliable estimates.

### 4.3 Specific star formation rates

As a further test whether our model predictions are in agreement within the observational limits, we compute the specific star formation rate (SSFR) for galaxies of a fixed stellar mass. Observationally, it is very difficult to infer the SSFR as a function of the $z = 0$ stellar mass since observations cannot connect galaxies at different epochs. Therefore it is not possible to follow the star formation history of an average galaxy across time with observations up to high redshift. However, it is possible to derive the average SSFR for galaxies within a stellar mass range at different redshifts. We can compare these observational data to the predictions of our model, by populating all haloes in a given snapshot with galaxies using our SHM relation to get stellar masses and our recipe for the star formation history to get their SFR. We show this comparison for low-mass galaxies with $\log(m_*/M_{\rm vir}) = 9.5$ in Figure 10 and for massive galaxies $\log(m_*/M_{\rm vir}) = 10.5$ in Figure 11. The comparison includes estimates derived from the UV (Feulner et al. 2005; Salim et al. 2007), the IR (Labbé et al. 2010; Schaerer & de Barros 2010; McLure et al. 2011), both UV and IR (Zheng et al. 2007; Noeske et al. 2007; Kajisawa et al. 2010), and from radio observations (Daddi et al. 2007; Dunne et al. 2009; Karim et al. 2011).

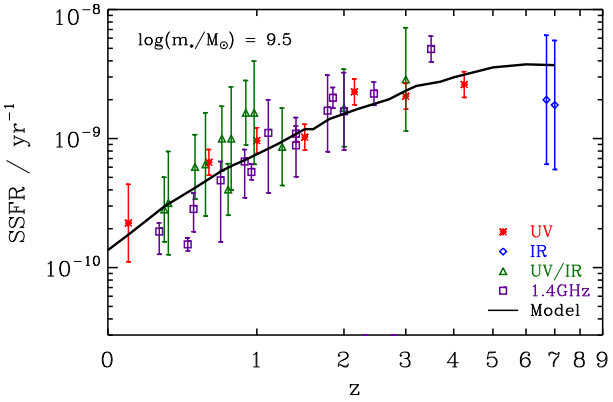


**Figure 10.** Specific star formation rate for galaxies with a stellar mass of $\log(m_*/M_{\rm vir}) = 9.5$ at the various epochs. The symbols of different colors give observational estimates derived with different methods and the black line is the result of our model. Although this relation has not been fit, the model is in excellent agreement with the data.

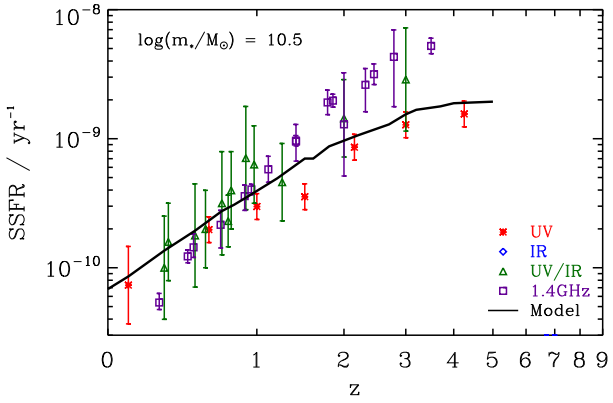


**Figure 11.** Same as Figure 10, but for galaxies with a stellar mass of $\log(m_*/M_{\rm vir}) = 10.5$ at the various epochs.

For both stellar mass ranges, our model is in excellent agreement with the data, although this relation has not been fit. This shows that mass-dependent quantities, such as the SSFR can be predicted up to high redshift in addition to global quantities such as the cosmic SFR density. As our model is able to fit a wide range of observed data, we are confident that it can be used to estimate reliably relations that cannot be easily observed, such as the star formation history of an average galaxy as a function its $z = 0$ halo mass.

## 5 DISCUSSION

In this study we draw conclusions on the assembly histories of galaxies over a wide range in mass from a conceptually simple approach matching observed galaxy mass functions and halo accretion histories from modern high resolution dark matter simulations which represent the underlying cosmological model. The early domination of in-situ star formation and the growing importance of late accretion of ex-situ stars for galaxies residing in more massive haloes found here is in good agreement with predictions from semi-analytical models (Kauffmann 1996; Khochfar & Silk 2006). Furthermore, our analysis confirms the results of De Lucia et al. (2006) who find using semi-analytic models that more massive (elliptical) galaxies have star formation histories that peak at higher redshifts than lower mass systems.

Although star formation ceases at low redshift for massive systems, the stellar mass of their central galaxies can grow considerably through accreted satellite galaxies. The majority of these ex-situ stars have formed when their galaxies still were centrals, i.e. before they entered the main halo. Therefore massive galaxies consist of old stellar populations. On the other hand, massive galaxies start to assemble very early due to star formation, but their final mass is assembled only very late. Employing semi-analytic models, De Lucia & Blaizot (2007) find that half of the mass of central galaxies of very massive haloes with $M_{\rm vir} = 10^{15} M_\odot$ forms after $z \sim 4$, but is locked up in the central galaxy only after $z = 0.5$. This is in good agreement with our results: extrapolating the 50 per cent assembly redshift in Figure 7 to $M_{\rm vir} = 10^{15} M_\odot$ roughly yields $z = 0.5$.

Our model indicates that low-mass (massive) galaxies form late (early), although their dark matter haloes assemble early (late). Although the haloes of low-mass galaxies assembles early it takes a considerable amount of time for the gas to cool and fall to the centre and form stars. In massive systems, on the other hand, the central galaxies (and the galaxies that will become satellites in these systems) can start to grow very early and form the bulk of their stars at high redshift. However, their haloes assemble only late, and the satellites are accreted onto the central galaxies at low redshift. Therefore, the stellar populations of massive galaxies are old, although massive haloes assemble late. This demonstrates that 'downsizing' is not anti-hierarchical, but a consequence of the bottom-up ΛCDM scenario (Neistein et al. 2006; Fontanot et al. 2009).

The contribution of star formation and accretion to the total stellar growth of central galaxies depends both on halo mass and redshift. While at high redshift accretion is negligible in all systems, at low redshift star formation dominates only in low-mass systems. The halo mass at which both processes contribute equally to the total growth of the central galaxy at $z = 0$ is $\log(M_{\rm vir}/M_\odot) \sim 12.7$, which corresponds to a stellar mass of $\log(m/M_\odot) \sim 10.9$. Here, both modes add $\sim 1 M_\odot$ yr$^{-1}$ to the stellar mass of the galaxy. This is in good agreement with the results of Guo & White (2008) who employ a semi-analytic model to study star formation and stellar accretion rates as a function of stellar mass and redshift. At $z = 0$ they find that the stellar mass of central galaxies for which both processes contribute equally is roughly $\log(m/M_\odot) \sim 10.6$, with rates of $\sim 0.5 - 1 M_\odot$ yr$^{-1}$ (see their Figure 3). For systems of lower (higher) mass, both methods indicate a lower (higher) contribution of ex-situ stars. At $z = 2$ the semi-analytic model predicts that the stellar mass of galaxies with an equal contribution of the two processes is roughly $\log(m/M_\odot) \sim 11.0$, with rates of $\sim 20 M_\odot$ yr$^{-1}$, while in our model only the most massive galaxies with $\log(m/M_\odot) \gtrsim 11.4$ have accretion rates that are comparable to their SFRs.

In the present study on average 50 per cent of the stars in galaxies in massive haloes ($10^{14} M_\odot$) at $z = 0$ are made in external galaxies and accreted at later epochs. However, in lower mass haloes, like that of the Milky Way ($10^{12} M_\odot$),

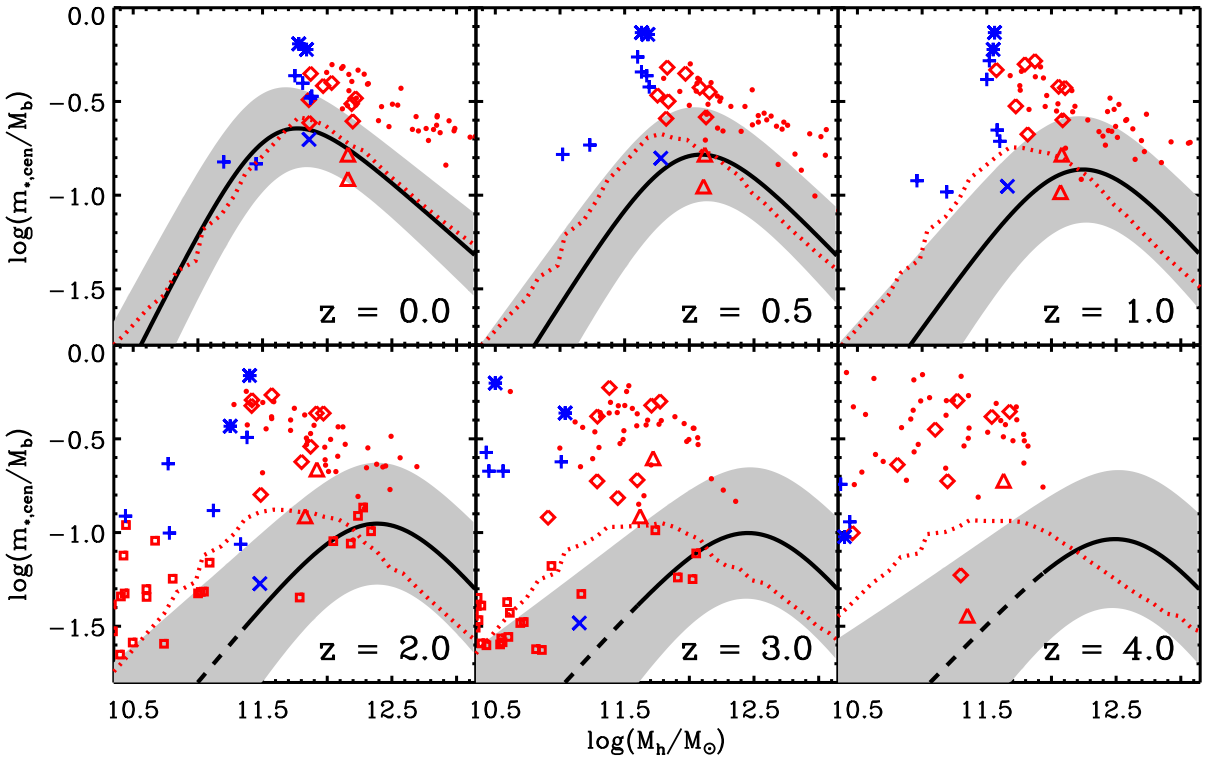


**Figure 12.** Comparison between central galaxy formation efficiencies found in numerical simulations at different redshifts. Each panel corresponds to the indicated redshift. The solid black lines give the average conversion efficiencies needed to fit the observed SMFs and the shaded areas indicate the $1\sigma$ confidence levels. The symbols show the results of hydrodynamical zoom-in simulations run with the GASOLINE code (blue asterisks: Brooks et al. 2011, pluses: Governato et al. 2012, crosses: Stinson et al. in prep.) and the GADGET code (red dots: Oser et al. 2010, diamonds: Scannapieco et al. 2011, squares: Genel et al. 2012, triangles: Okamoto 2012). The colored lines show the conversion efficiencies predicted by the semi-analytic model by Guo et al. (2011, red dotted line). While many simulations agree well with the predicted conversion efficiency at $z = 0$, most have too high values at earlier epochs, indicating that they form their stars too early.

this fraction is only a few per cent, making stellar accretion relatively unimportant for the evolution of the central galaxies. This in accord with standard formation and enrichment scenarios for disk galaxies (Matteucci & Francois 1989; Mo et al. 1998; Prantzos & Silk 1998; Naab & Ostriker 2006; Kauffmann et al. 2012).

Similar trends are reported from three-dimensional cosmological hydrodynamical zoom-in simulations, however, with larger fractions of accreted stars for galaxies of all masses. For the most massive galaxies this can be up to 80 per cent (Oser et al. 2010; Feldmann et al. 2010). Still, it is likely that this fraction is reduced to 50 percent (in the same mass bin) by the inclusion of strong stellar feedback which reduces the stellar content of the (typically lower mass) accreted galaxies (Hirschmann et al. 2012). In zoom-in simulations individual stellar particles can directly be followed and it has been shown that ex-situ stars predominantly assemble at larger radii (e.g. Laporte et al. 2012). In massive spheroidal galaxies, where the fraction of ex-situ stars is high, this material plays a significant role in the structural evolution of the galaxies (Naab et al. 2009; Hopkins et al. 2009; Feldmann et al. 2010; Oser et al. 2010, 2012). In lower-mass disk-like galaxies the accreted stars contribute to the build-up of the outer stellar halo and can also directly contribute on the order of 10 percent to the stellar mass of the disk (e.g. Abadi et al. 2006; Font et al. 2011; Tissera et al. 2012). Interestingly, these simulations predict ex-situ fractions of more than $\sim$ 20 per cent (up to 40-50 per cent) which is an order of magnitude higher then found in our study.

Our model constrains the mass budget of cosmological galaxy formation simulations not only at the present day but also at higher redshift. We compare our model to the results of hydrodynamical zoom-in simulations and semi-analytic models at six redshifts in Figure 12. While some older simulations have too high conversion efficiencies at $z = 0$, most of the newer simulations show good agreement with the efficiencies needed to reproduce the local observed SMFs. However, almost all simulations have far too high efficiencies at earlier epochs. This indicates that these simulations form too many stars early ($z \sim 3$), while at late times ($z \lesssim 2$) star formation is quenched too strongly, so that most of the stellar mass at $z = 0$ is already present at high redshift. The lack of late star formation in simulations could possibly explain the difficulties in getting prominent discs. Most stars are formed at times where processes leading to the formation of spheroids are common, e.g. major mergers or spin flips (Sales et al. 2011; Okamoto 2012). If the majority of stars form after these epochs, a more prominent disc forms.

The results of the semi-analytic models agree very well

with our relation at $z = 0$. This is not surprising as these models were tuned to fit the local SMF. At higher redshift however, their predictions differ from our model, indicating as noted in the original papers that they do not yield good fits to the observed high redshift SMFs. While the normalization and the slopes are in good agreement with our relation, the halo mass where the efficiency peaks ($M_1$), moves to lower masses with increasing redshift.

We note that a direct comparison between stellar masses measured in simulations and observed stellar masses is difficult. Especially at high redshift, it is complicated to estimate stellar masses observationally, as many different effects have to be taken into account. Moreover, one has to make a number of assumptions when fitting the spectral energy distributions (SEDs). An alternative way to compare stellar masses in models and observations is by making mock images of simulated galaxies using a stellar populations synthesis code and then obtaining a 'photometric' stellar mass with an SED fit. However there are two complications with this approach: First, it depends on the assumptions that are made to obtain the mock images (dust modeling, stellar populations synthesis modeling). Second, the reduction of the mock images would have to be done in the same way as for the observed data, which is non-trivial. Therefore we have decided to conduct a simpler comparison within the limits of the quoted observational errors.

The characteristic shape of the SHM relation is a consequence of several different physical processes, that prevent the gas in the dark matter halo from cooling (or reheat cold gas) and forming stars. The contribution of each process varies for systems of different mass. In low-mass systems, feedback from supernova-driven winds can be very effective as winds can easily expel large amounts of gas from haloes with low escape velocities (e.g. Larson 1974; Dekel & Silk 1986; Oppenheimer & Davé 2008; Puchwein & Springel 2012). Furthermore the amount of cooled gas is reduced by the presence of a UV and an X-ray background (Navarro & Steinmetz 1997; Gnedin 2000; Benson et al. 2002; Hambrick et al. 2011) and by cosmic rays (Jubelgas et al. 2008; Wadepuhl & Springel 2011). These effects have different efficiencies for different halo masses, such that the low-mass slope of the SHM relation can change at the halo mass, where the efficiencies of the two processes cross. However, with the current data it is very hard to find this transition mass, as the error estimates are even larger than the possible variations in the slope.

In massive haloes the star formation efficiency may be lowered by feedback from active galactic nuclei (AGN Springel et al. 2005; Croton et al. 2006; Bower et al. 2006; Somerville et al. 2008; Hambrick et al. 2011; Teyssier et al. 2011; Martizzi et al. 2012; Puchwein & Springel 2012) which can heat the gas in the halo and prevent it from cooling. Another effect that may be important for massive galaxies is gravitational heating (Khochfar & Ostriker 2008; Johansson et al. 2009). In hydrodynamical zoom-in simulations this effect is naturally included and results in a trend of lower galaxy formation efficiencies for more massive haloes, although still at levels which are significantly too high (Oser et al. 2010; Hirschmann et al. 2012). In this framework, the characteristic halo mass for which galaxy formation is most efficient is the mass where the combination of the various physical processes that reduce the efficiency is minimal. For massive galaxies the amount of in-situ stars is affected largely by processes that are effective for more massive systems (AGN feedback and gravitational heating), while the amount of ex-situ stars is strongly affected by processes that are effective for systems of lower mass (such as SN feedback and an ionizing background radiation).

Although the only observational constraints of our model are the observed SMFs from $z = 0$ to 4, our predictions for the evolution of the cosmic SFR density are in very good agreement with direct observation. This indicates that the evolution of the SMFs is consistent with the evolution of the cosmic SFR density, although the integrated observed SFR density was previously found to be higher than the observed stellar mass density (e.g. Hopkins & Beacom 2006). There are two effects that help to reconcile this tension. First, we employ the recent measurements by S12, who find a considerably steeper low-mass slope for the SMFs. This results in a larger amount of stellar mass in the low-mass end and thus increases the observed stellar mass density. Second, we include the effects of observational mass error in our model. As a consequence we find an evolution in the high-mass end of the 'true' SMFs, especially at low redshift. When both effects are taken into account, the tension between the evolution of the stellar mass density and the integrated SFR density is considerably lowered.

## 6 SUMMARY

In this paper, we present a galaxy evolution model that assumes a tight relation between the stellar mass of a galaxy and the mass of the dark matter halo in which it resides. With this approach we populate haloes with galaxies over the entire cosmic period from $z \sim 4$ to the present, using the $N$-body Millennium simulations and observed SMFs. Unlike the classical abundance matching technique our new method is self-consistent, taking into account that subhaloes are accreted at earlier times and with higher masses than when they are observed. We employ a redshift-dependent parameterization of the stellar-to-halo mass relation, and populate haloes and subhaloes with galaxies requiring that the observed SMFs at different redshifts be reproduced simultaneously.

We show that when observational mass errors are not taken into account, no consistent stellar mass evolution of massive galaxies can be obtained, as the central galaxy of a typical halo of mass $M_{\rm vir} = 10^{14} M_{\odot}$ would lose $\sim 25$ per cent of its stellar mass from $z = 1$ to 0. When we include observational mass errors, this tension vanishes and massive galaxies also have a physically consistent stellar mass evolution. We find that the halo mass where galaxy formation is most efficient is $\log(M_{\rm vir}/M_{\odot}) \sim 11.8$ at $z = 0$ and increases with increasing redshift to $\log(M_{\rm vir}/M_{\odot}) \sim 12.5$ at $z = 4$. Thus at high redshift, the peak efficiency of converting baryons into stars occurs in more massive haloes. The normalization of the SHM ratio decreases with increasing redshift: While at $z = 0$ the most efficient haloes have converted $\sim 23$ per cent of their baryons into stars, at $z = 4$ the peak efficiency is less than $\sim 10$ per cent.

We further compare our results to those of hydrodynamical zoom-in simulations and semi-analytic models and find that most of the newer models show good agreement

with the efficiencies needed to reproduce the local observed SMFs. However, almost all have efficiencies which are far too high at earlier epochs, indicating that they form their stars too early. At late times star formation is quenched, so that most of the stellar mass today is already present at high redshift. In the semi-analytic models the normalization and the slopes of the SHM relation are in good agreement with ours, but the halo mass where the efficiency peaks moves to lower rather than to higher masses with increasing redshift.

We then combine our relation with merger trees extracted from the simulations in order to predict the mean assembly histories of the stellar mass components within dark matter haloes (in situ and ex situ formation). We average over a sample of haloes with the same mass at $z = 0$, such that our model yields the average stellar mass growth of central galaxies as a function of halo mass. We find that in low-mass systems the halo grows much more slowly than its central galaxy. For a system with $M_{\rm vir} = 10^{12} M_{\odot}$, half of the stellar mass of the central galaxy forms after redshift $z = 0.7$ while half of the virial mass was already assembled by $z = 1.3$. For massive systems the trends are opposite at low redshift: the fractional growth of haloes is much stronger than stellar growth, while a large fraction of the stellar mass of massive galaxies is already in place early. For a system with $M_{\rm vir} = 10^{12} M_{\odot}$, half of the halo has assembled only by $z = 1.0$, but half of the stellar mass was already in place by $z = 1.8$. In very massive haloes with $M_{\rm vir} = 10^{12} M_{\odot}$ the galaxies start to form very early with 25 per cent of their stellar mass in place already by $z = 3.0$. However, it takes them a long time to fully assemble: Half of their stellar mass is in place only by $z = 1.6$, while 75 per cent of the stellar mass is in place by $z = 0.3$.

We then go further and identify the progenitors of a given halo at earlier epochs and derive the amount of stellar mass that has been accreted onto the central galaxy. Employing a recipe to account for mass loss from individual stars, we then compute the stellar mass that has been formed through star formation and convert this into a SFR. In this way we derive the SFR history as a function of halo mass. We find that the star formation history of central galaxies peaks at a certain redshift which depends on halo mass: for massive systems the peak occurs at high redshift while for low-mass systems it has not yet been reached by $z = 0$. After the peak has been reached, the SFR quickly drops, such that massive galaxies are quenched at $z \sim 2$. On the other hand, the stellar accretion rates increase with time for all systems. Massive systems have a high stellar accretion rate that dominates the total growth rate at late times, while for low-mass systems, accretion is insignificant at all times. The halo mass at which the accretion rate and the SFR are equal at $z = 0$ is $\log(M_{\rm vir}/M_{\odot}) \sim 12.7$.

Finally we demonstrate that our inferred SFR histories are in agreement with observation. We compute the SFR for all systems in the simulation and derive the evolution of the cosmic SFR density. Moreover we compute the specific SFR history for two different stellar mass ranges. We find that our choice for the parameterization of the redshift-dependent SHM relation is consistent with observational constraints, and that our inferred recipe for the mass dependent star formation histories gives reliable estimates.

**ACKNOWLEDGEMENTS**

We thank Alyson Brooks, Shy Genel, Fabio Governato, Qi Guo, Cheng Li, Takashi Okamoto, Ludwig Oser, Paola Santini, Cecilia Scannapieco, and Greg Stinson for providing their data in electronic form. The *MS* and *MS-II* were carried out at the Computing Centre of the Max Planck Society in Garching.

**REFERENCES**

Abadi M. G., Navarro J. F., Steinmetz M., 2006, MNRAS, 365, 747
Abazajian K. N., et al., 2009, ApJS, 182, 543
Angulo R. E., Springel V., White S. D. M., Jenkins A., Baugh C. M., Frenk C. S., 2012, ArXiv e-prints
Angulo R. E., White S. D. M., 2010, MNRAS, 405, 143
Baldry I. K., Glazebrook K., Driver S. P., 2008, MNRAS, 388, 945
Behroozi P. S., Conroy C., Wechsler R. H., 2010, ApJ, 717, 379
Bell E. F., McIntosh D. H., Katz N., Weinberg M. D., 2003, ApJS, 149, 289
Benson A. J., Lacey C. G., Baugh C. M., Cole S., Frenk C. S., 2002, MNRAS, 333, 156
Berlind A. A., Weinberg D. H., 2002, ApJ, 575, 587
Binney J., Tremaine S., 1987, Galactic dynamics. Princeton, NJ, Princeton University Press, 1987, 747 p.
Bouwens R. J., et al., 2009, ApJ, 705, 936
Bouwens R. J., et al., 2011, ArXiv e-prints
Bower R. G., Benson A. J., Malbon R., Helly J. C., Frenk C. S., Baugh C. M., Cole S., Lacey C. G., 2006, MNRAS, 370, 645
Boylan-Kolchin M., Ma C.-P., Quataert E., 2008, MNRAS, 383, 93
Boylan-Kolchin M., Springel V., White S. D. M., Jenkins A., Lemson G., 2009, MNRAS, 398, 1150
Brooks A. M., et al., 2011, ApJ, 728, 51
Brown M. J. I., et al., 2008, ApJ, 682, 937
Bruzual G., Charlot S., 2003, MNRAS, 344, 1000
Castellano M., et al., 2010, A&A, 511, A20
Chabrier G., 2003, PASP, 115, 763
Cole S., et al., 2001, MNRAS, 326, 255
Conroy C., Wechsler R. H., 2009, ApJ, 696, 620
Conroy C., Wechsler R. H., Kravtsov A. V., 2006, ApJ, 647, 201
Conroy C., Wechsler R. H., Kravtsov A. V., 2007, ApJ, 668, 826
Crain R. A., et al., 2009, MNRAS, 399, 1773
Croton D. J., Springel V., White S. D. M., De Lucia G., Frenk C. S., Gao L., Jenkins A., Kauffmann G., Navarro J. F., Yoshida N., 2006, MNRAS, 365, 11
Cucciati O., et al., 2012, A&A, 539, A31
Daddi E., et al., 2007, ApJ, 670, 156
De Lucia G., Blaizot J., 2007, MNRAS, 375, 2
De Lucia G., Springel V., White S. D. M., Croton D., Kauffmann G., 2006, MNRAS, 366, 499
Dekel A., Silk J., 1986, ApJ, 303, 39
Drory N., Salvato M., Gabasch A., Bender R., Hopp U., Feulner G., Pannella M., 2005, ApJL, 619, L131
Dunne L., et al., 2009, MNRAS, 394, 3

Fall S. M., Efstathiou G., 1980, MNRAS, 193, 189
Fazio G. G., et al., 2004, ApJS, 154, 10
Feldmann R., Carollo C. M., Mayer L., Renzini A., Lake G., Quinn T., Stinson G. S., Yepes G., 2010, ApJ, 709, 218
Feulner G., Gabasch A., Salvato M., Drory N., Hopp U., Bender R., 2005, ApJL, 633, L9
Font A. S., McCarthy I. G., Crain R. A., Theuns T., Schaye J., Wiersma R. P. C., Dalla Vecchia C., 2011, MNRAS, 416, 2802
Fontana A., et al., 2006, A&A, 459, 745
Fontanot F., De Lucia G., Monaco P., Somerville R. S., Santini P., 2009, MNRAS, 397, 1776
Genel S., et al., 2012, ApJ, 745, 11
Gnedin N. Y., 2000, ApJ, 542, 535
Governato F., et al., 2012, MNRAS, p. 2697
Guo Q., et al., 2011, MNRAS, 413, 101
Guo Q., White S., Li C., Boylan-Kolchin M., 2010, MNRAS, 404, 1111
Guo Q., White S. D. M., 2008, MNRAS, 384, 2
Hambrick D. C., Ostriker J. P., Johansson P. H., Naab T., 2011, MNRAS, 413, 2421
Hatton S., Devriendt J. E. G., Ninin S., Bouchet F. R., Guiderdoni B., Vibert D., 2003, MNRAS, 343, 75
Hirschmann M., Naab T., Somerville R. S., Burkert A., Oser L., 2012, MNRAS, 419, 3200
Hopkins A. M., Beacom J. F., 2006, ApJ, 651, 142
Hopkins P. F., Hernquist L., Cox T. J., Keres D., Wuyts S., 2009, ApJ, 691, 1424
Johansson P. H., Naab T., Ostriker J. P., 2009, ApJL, 697, L38
Jubelgas M., Springel V., Enßlin T., Pfrommer C., 2008, A&A, 481, 33
Kajisawa M., Ichikawa T., Yamada T., Uchimoto Y. K., Yoshikawa T., Akiyama M., Onodera M., 2010, ApJ, 723, 129
Kang X., Jing Y. P., Mo H. J., Börner G., 2005, ApJ, 631, 21
Karim A., et al., 2011, ApJ, 730, 61
Katz N., Weinberg D. H., Hernquist L., 1996, ApJS, 105, 19
Kauffmann G., 1996, MNRAS, 281, 487
Kauffmann G., Colberg J. M., Diaferio A., White S. D. M., 1999, MNRAS, 303, 188
Kauffmann G., Li C., Fu J., Saintonge A., Catinella B., Tacconi L. J., Kramer C., Genzel R., Moran S., Schiminovich D., 2012, MNRAS, 422, 997
Kereš D., Katz N., Weinberg D. H., Davé R., 2005, MNRAS, 363, 2
Khochfar S., Ostriker J. P., 2008, ApJ, 680, 54
Khochfar S., Silk J., 2006, MNRAS, 370, 902
Klypin A. A., Trujillo-Gomez S., Primack J., 2011, ApJ, 740, 102
Komatsu E., et al., 2011, ApJS, 192, 18
Labbé I., et al., 2010, ApJL, 716, L103
Laporte C. F. P., White S. D. M., Naab T., Ruszkowski M., Springel V., 2012, ArXiv e-prints
Larson R. B., 1974, MNRAS, 169, 229
Leauthaud A., et al., 2012, ApJ, 746, 95
Li C., White S. D. M., 2009, MNRAS, 398, 2177
Ly C., Lee J. C., Dale D. A., Momcheva I., Salim S., Staudaher S., Moore C. A., Finn R., 2011, ApJ, 726, 109
Martizzi D., Teyssier R., Moore B., Wentz T., 2012, MNRAS, p. 2773
Matteucci F., Francois P., 1989, MNRAS, 239, 885
McLure R. J., et al., 2011, MNRAS, 418, 2074
Mo H. J., Mao S., White S. D. M., 1998, MNRAS, 295, 319
Moster B. P., Maccio' A. V., Somerville R. S., Naab T., Cox T. J., 2011, ArXiv e-prints
Moster B. P., Somerville R. S., Maulbetsch C., van den Bosch F. C., Macciò A. V., Naab T., Oser L., 2010, ApJ, 710, 903
Moster B. P., Somerville R. S., Newman J. A., Rix H.-W., 2011, ApJ, 731, 113
Naab T., Burkert A., 2003, ApJ, 597, 893
Naab T., Johansson P. H., Ostriker J. P., 2009, ApJL, 699, L178
Naab T., Ostriker J. P., 2006, MNRAS, 366, 899
Navarro J. F., Steinmetz M., 1997, ApJ, 478, 13
Neistein E., van den Bosch F. C., Dekel A., 2006, MNRAS, 372, 933
Nipoti C., Londrillo P., Ciotti L., 2003, MNRAS, 342, 501
Noeske K. G., et al., 2007, ApJL, 660, L47
Okamoto T., 2012, ArXiv e-prints
Oppenheimer B. D., Davé R., 2008, MNRAS, 387, 577
Oppenheimer B. D., Davé R., Kereš D., Fardal M., Katz N., Kollmeier J. A., Weinberg D. H., 2010, MNRAS, 406, 2325
Oser L., Naab T., Ostriker J. P., Johansson P. H., 2012, ApJ, 744, 63
Oser L., Ostriker J. P., Naab T., Johansson P. H., Burkert A., 2010, ApJ, 725, 2312
Panter B., Jimenez R., Heavens A. F., Charlot S., 2007, MNRAS, 378, 1550
Peacock J. A., Smith R. E., 2000, MNRAS, 318, 1144
Pérez-González P. G., et al., 2008, ApJ, 675, 234
Prantzos N., Silk J., 1998, ApJ, 507, 229
Puchwein E., Springel V., 2012, ArXiv e-prints
Robotham A. S. G., Driver S. P., 2011, MNRAS, 413, 2570
Rujopakarn W., et al., 2010, ApJ, 718, 1171
Sales L. V., Navarro J. F., Theuns T., Schaye J., White S. D. M., Frenk C. S., Crain R. A., Dalla Vecchia C., 2011, ArXiv e-prints
Salim S., et al., 2007, ApJS, 173, 267
Santini P., et al., 2012, A&A, 538, A33
Scannapieco C., White S. D. M., Springel V., Tissera P. B., 2011, MNRAS, 417, 154
Schaerer D., de Barros S., 2010, A&A, 515, A73
Schaye J., et al., 2010, MNRAS, 402, 1536
Shankar F., Lapi A., Salucci P., De Zotti G., Danese L., 2006, ApJ, 643, 14
Smolčić V., et al., 2009, ApJ, 690, 610
Somerville R. S., Hopkins P. F., Cox T. J., Robertson B. E., Hernquist L., 2008, MNRAS, 391, 481
Spergel D. N., et al., 2003, ApJS, 148, 175
Springel V., et al., 2005, Nature, 435, 629
Springel V., Hernquist L., 2003, MNRAS, 339, 289
Springel V., White S. D. M., Tormen G., Kauffmann G., 2001, MNRAS, 328, 726
Teyssier R., Moore B., Martizzi D., Dubois Y., Mayer L., 2011, MNRAS, 414, 195
Tinker J. L., Weinberg D. H., Zheng Z., Zehavi I., 2005, ApJ, 631, 41

Tissera P. B., White S. D. M., Scannapieco C., 2012, MNRAS, 420, 255
Trenti M., Stiavelli M., 2008, ApJ, 676, 767
Vale A., Ostriker J. P., 2004, MNRAS, 353, 189
Vale A., Ostriker J. P., 2006, MNRAS, 371, 1173
van den Bosch F. C., Yang X., Mo H. J., 2003, MNRAS, 340, 771
van der Burg R. F. J., Hildebrandt H., Erben T., 2010, A&A, 523, A74
Wadepuhl M., Springel V., 2011, MNRAS, 410, 1975
Wake D. A., et al., 2011, ApJ, 728, 46
Werner M. W., et al., 2004, ApJS, 154, 1
White M., 2001, MNRAS, 321, 1
White M., Zheng Z., Brown M. J. I., Dey A., Jannuzi B. T., 2007, ApJL, 655, L69
White S. D. M., Rees M. J., 1978, MNRAS, 183, 341
Windhorst R. A., et al., 2011, ApJS, 193, 27
Yang X., Mo H. J., van den Bosch F. C., 2003, MNRAS, 339, 1057
Yang X., Mo H. J., van den Bosch F. C., Zhang Y., Han J., 2011, ArXiv e-prints
York D. G., et al., 2000, AJ, 120, 1579
Zehavi I., et al., 2004, ApJ, 608, 16
Zehavi I., et al., 2011, ApJ, 736, 59
Zheng X. Z., Bell E. F., Papovich C., Wolf C., Meisenheimer K., Rix H.-W., Rieke G. H., Somerville R., 2007, ApJL, 661, L41